Highly supercooled riming and unusual triple-frequency radar signatures over Antarctica

Frederic Tridon[1,*], Israel Silber[2], Alessandro Battaglia[3,4], Stefan Kneifel[1], Ann Fridlind[5], Petros Kalogeras[4], and Ranvir Dhillon[4]

[1]Institute for Geophysics and Meteorology, University of Cologne, Cologne, Germany
[2]Department of Meteorology and Atmospheric Science, Pennsylvania State University, University Park, PA, USA
[3]DIATI, Politecnico di Torino, Turin, Italy
[4]University of Leicester, Leicester, UK
[5]NASA Goddard Institute for Space Studies, New York, NY, USA
[*]Now at: DIATI, Politecnico di Torino, Turin, Italy

Correspondence: frederic.tridon@polito.it

Abstract. Riming of ice crystals by supercooled water droplets is an efficient ice growth process, but its basic properties are still poorly known. While it has been shown to contribute significantly to surface precipitation at mid-latitudes, little is known about its occurrence at high latitudes. In Antarctica, two competing effects can influence the occurrence of riming: the scarcity of supercooled liquid water clouds due to the extremely low tropospheric temperatures and the low aerosol concentration, which may lead to the formation of fewer and larger supercooled drops potentially resulting in an enhanced riming efficiency.

In this work, by exploiting the deployment of an unprecedented number of multi-wavelength active and passive remote sensing systems (including triple-frequency radar measurements) in West Antarctica, during the Atmospheric Radiation Measurements West Antarctic Radiation Experiment (AWARE) field campaign, we evaluate the importance of riming incidence in Antarctica and find that riming occurs at much lower temperatures compared to the mid-latitudes.

We then focus on a case study featuring a persistent layer of unexpectedly pronounced triple-frequency radar signatures but only a relatively modest amount of supercooled liquid water. In-depth analysis of the radar observations suggests that such signatures can only be explained by the combined effects of moderately rimed aggregates or similarly shaped florid polycrystals and a narrow particle size distribution (PSD). Simulations of this case study performed with a 1D bin model indicate that similar triple frequency radar observations can be reproduced when narrow PSDs are simulated. Such narrow PSDs can in turn be explained by two key factors: (i) the presence of a shallow homogeneous droplet or humidified aerosol freezing layer aloft seeding an underlying supercooled liquid layer, and (ii) the absence of turbulent mixing throughout a stable polar atmosphere that sustains narrow PSDs, as hydrometeors grow from the nucleation region aloft to several millimeter ice particles, by vapor deposition and then riming.

1 Introduction

Besides deposition and aggregation, riming is an efficient ice growth process. It contributes significantly to surface precipitation at mid-latitudes (Grazioli et al., 2015; Moisseev et al., 2017) and is pivotal for improving our understanding of the role of

ice phase in the water budget. However, basic properties of riming such as its efficiency or its importance in precipitation formation are still largely unknown since it involves the collection of poorly characterized supercooled water droplets by complex ice particles. It is widely accepted, however, that at the beginning of a riming process, the mass of a rimed ice particle

25 increases while its maximum dimension remains constant or only slightly increases (e.g., Heymsfield, 1982; Seifert et al., 2019); hence, the density and fall speed of rimed ice hydrometeors tend to be enhanced. Riming occurrence is strongly linked with temperature since the probability of finding supercooled liquid water decreases with temperature. By exploiting a multi-year dataset of cloud radar observations at four European sites in various environment, Kneifel and Moisseev (2020) showed that riming is rare below -12°C and more frequent closer to 0°C.

30 In the Arctic, supercooled liquid water clouds are frequent (e.g., Shupe et al., 2008; Cesana et al., 2012; Morrison et al., 2012; Mioche et al., 2015) and rimed precipitating particles are commonly observed (Mioche et al., 2017; Fitch and Garrett, 2022). In Antarctica however, liquid water clouds are less frequent, in particular during winter months due to lower temperatures (e.g., Matus and L'Ecuyer, 2017; Lubin et al., 2020). Nevertheless, the typical low aerosol concentrations in this region can lead to the formation and persistence of supercooled drizzle drops (Silber et al., 2019a), which might facilitate the occurrence of

35 riming due to the enhanced riming efficiency of drizzle drops (Lohmann, 2004). Therefore, a thorough investigation of riming in Antarctic clouds is timely.

Field measurements in Antarctica are historically sparse due to logistical challenges. Space-borne instruments such as the Cloud Profiling Radar (CPR) onboard CloudSat (Stephens et al., 2008) can cover extended and remote areas but have inherent limitations to measure weak ice precipitation fluxes (e.g., Silber et al., 2021), or any ice precipitation fluxes near the ground

40 due to the so-called "blind-zone" (Maahn et al., 2014). Only recently, riming has been shown to be a recurring process at an Antarctic site based on ground-based optical probe observations at the Dumont d'Urville Station (Grazioli et al., 2017), with most of the detected large ice hydrometeors being at least partially rimed. However, in order to detect an active riming process, suitable measurement are needed across the vertical column, which can be achieved via ground-based multi-frequency radars, for example.

45 By analysing scattering models of snow aggregates and graupel, Kneifel et al. (2011) suggested that triple-frequency radar measurements could be exploited to differentiate between rimed and unrimed ice particles. This differentiation has been later verified by comparing triple-frequency radar signatures with bulk snow density derived from collocated ground-based observations (Kneifel et al., 2015). While the radar Doppler velocity is the simplest and most obvious parameter for retrieving the degree of riming or an equivalent parameter (e.g. density factor or rime mass fraction) of ice particles (e.g., Mosimann, 1995;

50 Mason et al., 2018; Kneifel and Moisseev, 2020), triple frequency radar observations can also provide critical information on the internal structure of snowflakes (Mason et al., 2019), and hence, on the growth processed involved. For example, by exploiting triple-frequency Doppler spectra, Kneifel et al. (2016) combined triple-frequency and Doppler velocity information and confirmed that rimed and unrimed aggregates produce distinct scattering signatures. Further development of multi-frequency radar retrievals demonstrated that the combination of three radar frequencies enables the derivation of snow aggregate properties with various degree of riming (e.g., Mason et al., 2018). Quantitative agreement was found with the measurements from

collocated ground-based (Moisseev et al., 2017; von Lerber et al., 2017) or airborne (Leinonen et al., 2018; Tridon et al., 2019) in-situ probes.

In the framework of the Atmospheric Radiation Measurement (ARM) West Antarctic Radiation Experiment (AWARE, Lubin et al., 2020), the U.S. Department of Energy (DOE) deployed the second ARM Mobile Facility (AMF2) at McMurdo

60 Station from 1 December 2015 to 31 December 2016, resulting in an unprecedented suite of remote sensing instruments in Antarctica, including the Ka-band ARM Zenith Radar (KAZR), the Marine W-band ARM Cloud Radar (MWACR) and the scanning dual-wavelength ARM cloud radar system (X/KaSACR). Although the MWCAR stopped transmitting after about three months, these instruments provided triple-wavelength radar profiles for the first time in Antarctica (in Sect. 2). In this work these data have been exploited to evaluate the probability of finding triple-frequency signatures of riming in clouds over

65 McMurdo Station and have been compared with climatologies collected at other triple-frequency radar sites at mid-latitudes and in the Arctic (Sect. 3). A case study with strong triple-frequency signatures is further analysed in Sect. 4 via a detailed retrieval of ice microphysics, and bin model simulations performed to investigate its salient features. Conclusions are drawn in Sect. 5.

2   Radar Data processing

70 KAZR, MAWCR, radiosonde and XSACR data (Atmospheric Radiation Measurement (ARM) user facility, 2014, 2015a, b, c, respectively) were collected during the AWARE field campaign at McMurdo Station located at the southern tip of Ross Island, Antarctica (77°50'47"S, 166°40'06"E, 76 m above mean sea level; see Fig. 2a).

While the KAZR and MWACR are zenith-pointing radars, the X/KaSACR loops through a sequence of various scanning modes in order to sample the three-dimensional geometry of clouds (Kollias et al., 2014), including a zenith-pointing period

75 of about 25 min every 2 hours. Triple-frequency radar observations are therefore available only during these zenith-pointing operation periods. At the beginning of the field campaign, the radar beams alignment has been maximized for an optimal volume matching. Since the temporal and range resolution of the radars slightly differ, their data have been first regridded to a common 3 s by 30 m time–height grid.

Following standard ARM procedures, absolute calibrations of the scanning radar systems have been performed on site with

80 a corner reflector and the calibration of the KaSACR has been transferred to the KAZR via a statistical comparison of the reflectivities measured in the vertical (Kollias et al., 2016, 2020). Without the possibility to use natural volume targets, such as rainfall, for checking the radar calibration (e.g. involving a co-located disdrometer as in Dias Neto et al., 2019), the calibration cannot be considered to be more accurate than ± 3 dB and absolute reflectivities are mainly used qualitatively in the current study. The KAZR calibration provided in the ARM Archive was deemed appropriate despite the results from Kollias et al.

85 (2019), based on a systematic comparison with nearby measurements from Cloudsat, suggesting a rather large miscalibration of the KAZR during AWARE. Indeed, such an automatic method is challenging in an area with complex topography like McMurdo and, for the AWARE campaign, it suggests an erratic KAZR calibration instability with an offset ranging between

Table 1. List of AWARE cases with triple frequency radar observations.

Start time [UTC]	End time [UTC]	Cloud top [km AGL]	Duration with 3-frequency [min]
31/12/2015 17:00	01/01/2016 21:00	3.5	46
02/01/2016 10:00	05/01/2016 09:00	6	351
09/01/2016 23:00	11/01/2016 15:00	8	117
16/01/2016 13:00	21/01/2016 07:00	7	339
28/01/2016 14:00	01/02/2016 17:00	6	172
02/02/2016 18:00	03/02/2016 08:00	6	86
08/02/2016 18:00	12/02/2016 09:00	5	180

3.5 and 7.7 dB. Furthermore, thanks to coincidental observations during the case study presented in Sect. 4, comparisons of KAZR and Cloudsat reflectivities suggest the ARM calibration to be appropriate.

Before deriving the dual-wavelength ratios (DWRs), the relative calibration between the different radars is performed. Firstly, the two-way attenuation profile due to atmospheric gases is derived from the measurements of the closest radio soundings and the absorption model of Rosenkranz (1998). Secondly, the remaining offsets due to supercooled liquid, snow, and radome attenuation as well as possible absolute calibration differences are derived by matching the measured reflectivity near cloud tops, where only small hydrometeors are present and non-Rayleigh scattering is negligible (Tridon et al., 2020). While the XSACR calibration proposed in the ARM Archive was found to be correct, a considerable offset of +19.6 dB was necessary for the MWACR.

Due to a failed power supply, the MWACR was taken offline in March 2016 (Lubin et al., 2017) and the triple-frequency dataset is limited to only about three months. Nevertheless, during this period 7 multi-day snowfall events were recorded during which the signal to noise ratio of all three radars exceeded -10 dB. This results in a total duration of 21 hours of triple frequency observations (see Table 1), providing insights on how frequent riming might be in Antarctica, at least for the summer season.

3 Triple-frequency signatures during AWARE

3.1 Results from previous data sets

In order to highlight the occurrence of aggregation or riming processes, it is helpful to combine the DWRs of all three frequencies in a single plot showing $DWR_{X,Ka}$ as function of $DWR_{Ka,W}$, as proposed by Kneifel et al. (2011). When snowflakes become sufficiently large (with a threshold on the characteristic sizes that depend on the frequency pair; see Fig. A4 in Battaglia et al., 2020a), their reflectivity depends on the radar frequency and the DWRs depart from zero. In a nutshell, the $DWR_{X,Ka}$ and $DWR_{Ka,W}$ increase almost equally in case of aggregates, while the $DWR_{X,Ka}$ remains much lower than $DWR_{Ka,W}$ in case of rimed particles (a maximum $DWR_{X,Ka}$ of roughly 3 dB was suggested by Kneifel et al., 2015; Dias Neto et al., 2019,

but it can reach slightly larger values when the mean mass diameter is larger than 3 mm). The proposed explanation for this

110 behaviour is that the rimed particles are too small to enhance the $\mathrm{DWR}_{X,Ka}$ while their larger density enhance their refractive index, and hence, the $\mathrm{DWR}_{Ka,W}$ (Dias Neto et al., 2019). In case of very large low-density aggregates, the $\mathrm{DWR}_{Ka,W}$ can actually decrease producing a bending back of the curve (for details, see Kneifel et al., 2015). Mason et al. (2019) have shown that the shape of the size distribution and the internal structure of snowflakes also have a non-negligible influence on the triple-frequency signatures.

115 The ARM program has pioneered ground-based triple-frequency radar observations (e.g., during the BAECC field campaign, Petäjä et al., 2016) and similar experimental setups are emerging at other sites such as the TRIple-frequency and Polarimetric radar experiment (TRIPEx) at the Jülich Observatory for Cloud Evolution, Germany (Dias Neto et al., 2019). The triple-frequency density occurrence derived from datasets collected at these sites generally include the branches of both aggregates and rimed particles (Kneifel et al., 2015; Mason et al., 2018, 2019; Dias Neto et al., 2019). This is also true for the AWARE

120 snowfall event on the 10th of January which was succinctly analysed in Lubin et al. (2020). A peculiarity of the AWARE case analysed in the current paper (see Sect. 4) is the presence of a rimed particle branch leading to very large $\mathrm{DWR}_{Ka,W}$ values (up to 16 dB); $\mathrm{DWR}_{Ka,W}$ barely exceeds 12 dB for all other studies cited above and corresponding to data from various sites located at mid to high latitudes.

3.2 Temperature dependence of DWRs

125 In order to investigate the conditions at which the aggregation and riming processes occur, another way of showing the triple-frequency signatures is to plot the profiles of the observed DWRs after they have been stratified according to air temperature (Fig. 1a,b), as suggested by Dias Neto et al. (2019) for their TRIPEx dataset. To this aim, the temperature information has been interpolated from the closest radio soundings, which were launched every 12 hours during AWARE. For comparison, this has also been applied to the BAECC triple-frequency dataset (Fig. 1c,d) which has already been thoroughly analysed in previous

130 papers (e.g., Kneifel et al., 2015; Mason et al., 2018, 2019). The BAECC DWR density plots are practically identical to those from TRIPEx (Fig. 9 in Dias Neto et al., 2019), two sites which can be identified as mid-latitudes.

Despite appearing slightly noisier due to the reduced size of the data set, the AWARE density plots (Fig. 1) show interesting similarities in comparison with those from BAECC (and, equivalently, TRIPEx), but also some striking differences. On the similarities side, the medians of both DWRs (black lines) reach nearly the same maxima around 0°C (6 and 2 dB for $\mathrm{DWR}_{Ka,W}$

135 and $\mathrm{DWR}_{X,Ka}$, respectively). Furthermore, the rate of increase of the $\mathrm{DWR}_{X,Ka}$ with temperature is similar: it remains small at low temperatures and increases faster for temperatures greater than -15°C, which can be explained by a rapid growth of aggregates favored by the dendritic growth around -15°C. On the disparities side, the AWARE $\mathrm{DWR}_{Ka,W}$ increases at a lower temperature (around -25°C) compared to the mid-latitude sites. Furthermore, there is a thin but striking branch of $\mathrm{DWR}_{Ka,W}$ reaching extreme values, much higher than the common maximum of 12 dB, a feature which is consistent with the triple-

140 frequency signatures shown in Lubin et al. (2020).

It appears somewhat unlikely that the aggregation process has a temperature dependence which would be different from mid-latitudes because the shape of ice particles is mainly a result of temperature and supersaturation (e.g., Bailey and Hallett,
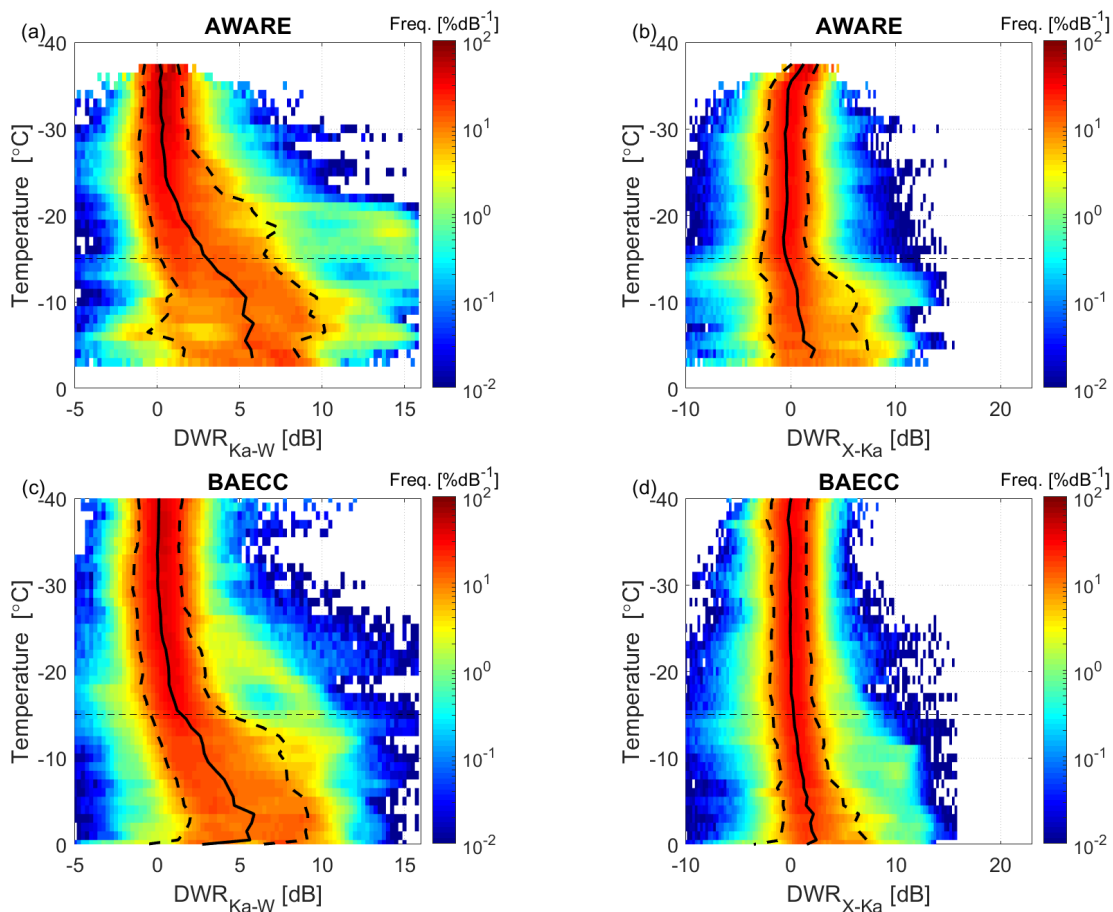
Figure 1. Density plots of DWR$_{Ka-W}$ (a,c) and DWR$_{X-Ka}$ (b,d) as function of temperature for AWARE (a,b) and BAECC (c,d) datasets. The dashed lines indicate the 10th and 90th percentiles.

2009). In our opinion, a much more likely explanation for the increase of DWR$_{Ka,W}$ at low temperatures might be occurrence of riming at lower temperatures. This differences from previous studies may be explained by the low concentration of aerosol in Antarctica, compared to the northern hemisphere: a low cloud condensation nuclei concentration could lead to fewer but larger supercooled droplets (for a given cloud water content), and therefore, more efficient riming (Lohmann, 2004). In the rest of the paper, this interpretation will be further assessed by focusing on a single case study, which features the strongest DWR$_{Ka,W}$ of the AWARE dataset.
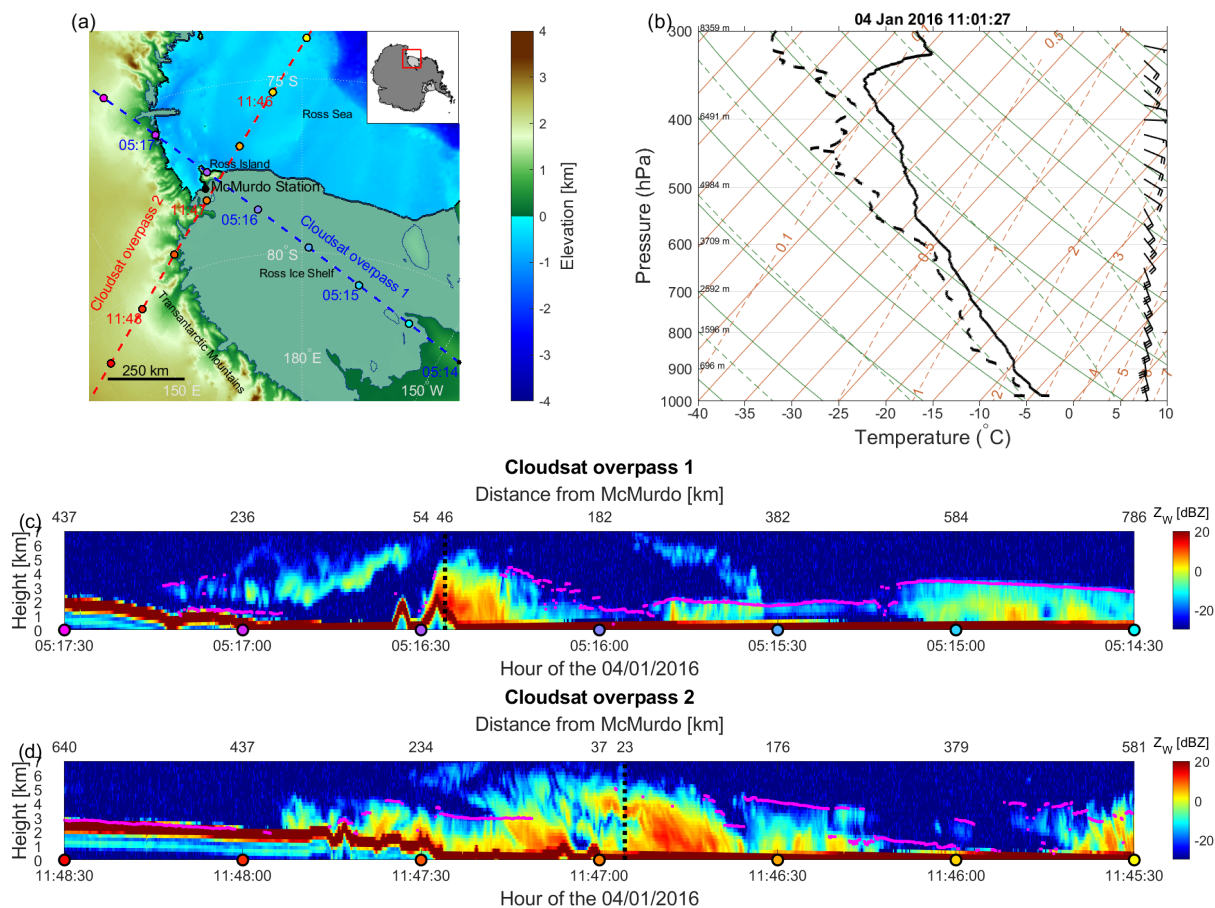
Figure 2. (a) Overview of the geographical features around McMurdo. (b) Atmospheric (continuous line) and dew point (dashed line) temperatures profiles measured by the 10:24 UTC sounding from the AMF2 on the 4th of January. Time-height cross sections of the reflectivity measured during the ascending (c) and descending (d) Cloudsat overpasses closest to McMurdo for the same day, indicated by the blue and red dashed lines in (a) (the colored circles in (a) and along the x-axis of (c) (d) are spaced by 30 s timesteps along the satellite path (equivalent to 228 km) and allow to better visualize the position of the cloud system). The vertical black dotted lines in (c) and (d) show the time of the closest approach for each overpass, and magenta lines indicate supercooled liquid water clouds as detected by CALIPSO.

4 Extreme triple-frequency signatures of the 4th January 2016

4.1 General description of the case study

Between the 1st and 4th January 2016, the weather conditions were typical of the frequent strong katabatic wind events recorded at McMurdo Station (Chenoli et al., 2013; Coggins et al., 2014; Monaghan et al., 2005; Weber et al., 2016). The Ross sea semi-permanent cyclonic circulation (Carrasco and Bromwich, 1994; Monaghan et al., 2005; Simmonds et al., 2003) deepened and moved to the South, bringing moist air over the Ross Ice Shelf (see Fig. 2a). MODIS cloud phase retrieval (see Fig. 3) indicates that clouds formed over the ice shelf, including extended clouds with supercooled liquid at their top. The evolution of cloud features in the subsequent panels of Fig. 3 demonstrates the cyclonic (clockwise) circulation centered around the North of the Ross ice shelf, which led to deeper ice-topped clouds along the Transantarctic Mountains to the West of the Ross ice shelf (see Fig. 2c,d). Cloud initiation mechanisms included lifting of air due to the relief barrier and convergence of cyclone winds with katabatic winds descending from the Antarctic Plateau. Between the 2nd and 4th of January, this resulted in strong Southerly winds (e.g. winds up to $16\,\mathrm{m\,s^{-1}}$ were recorded at $1.7\,\mathrm{km}$ ASL by the radiosonde launched from the AMF2 at McMurdo on the 4th of January at 11h UTC as shown in Fig. 2b) associated with long lasting clouds deepening on the windward side of Ross Island.

On the 4th January 2016, Cloudsat made two overpasses exceptionally close to McMurdo Station (as close as 46 and $23\,\mathrm{km}$ at 5:16 and 11:47 UTC, respectively). Cloudsat reflectivity transects (Figs. 2c and d) confirm the presence of extended and complex cloud fields over the whole Ross Ice Shelf, and particularly deep clouds near McMurdo with cloud tops reaching nearly $6\,\mathrm{km}$ ASL and reflectivity as large as 14 dBZ. Furthermore, co-located CALIPSO observations indicate that most of these clouds were mixed-phase clouds with a supercooled liquid layer at their tops at temperatures as low as -35°C (magenta lines in Figs. 2c and d).

4.2 Observations at McMurdo

Over McMurdo, a persistent thick cloud layer was continuously observed between the 2nd and 5th January 2016. While the ARM lidars were not able to penetrate through the full extent of the clouds and sample their top, the associated liquid cloud base height products (Silber et al., 2018a, b) suggest that supercooled liquid layers were almost always present at various heights within the clouds, from 0.5 to $3\,\mathrm{km}$ AGL (not shown).

Of particular interest on the 4th of January is the period between 07 and 12 UTC which is associated with a persistent supercooled liquid layer around $2\,\mathrm{km}$ AGL and characterised by clouds with the largest reflectivities (Fig. 4a). After applying the climatological relative calibrations determined for the whole AWARE field campaign (see Sect. 2), effective $\mathrm{DWR}_{X,Ka}$ and $\mathrm{DWR}_{Ka,W}$ are derived (Fig. 4c and e, respectively).

Microwave radiometer measurements were not available at McMurdo before the 29th of January 2016. Before that date, liquid water path can still be roughly estimated thanks to multi-frequency radar observations (Tridon et al., 2020): using the Rayleigh plateau technique, Rayleigh reflectivity regions at cloud top can be identified (non-shaded zones in Fig. 4e) and used to derive the two-way differential path-integrated attenuation (ΔPIA, black thick line at the top of Fig. 4e associated
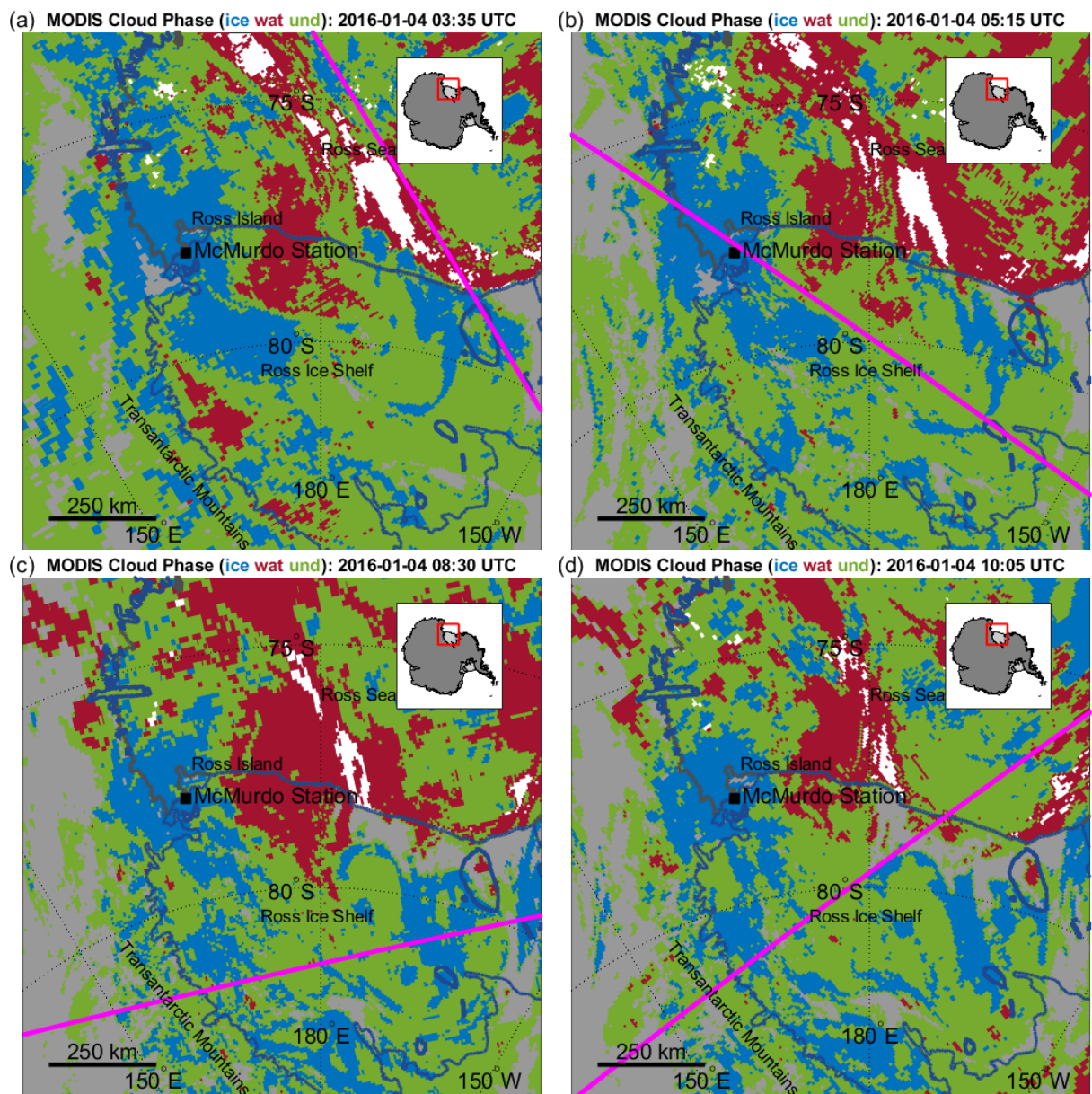
Figure 3. Time evolution of cloud top phase (ice, liquid or undetermined in blue, red and green, respectively) retrieved by subsequent MODIS overpasses on the 4th of January at (a) 3:35, (b) 5:15, (c) 8:30 and (d) 10:05 UTC within the geographical area shown in Fig. 2a. The magenta lines correspond to the satellite ground track for each overpass.
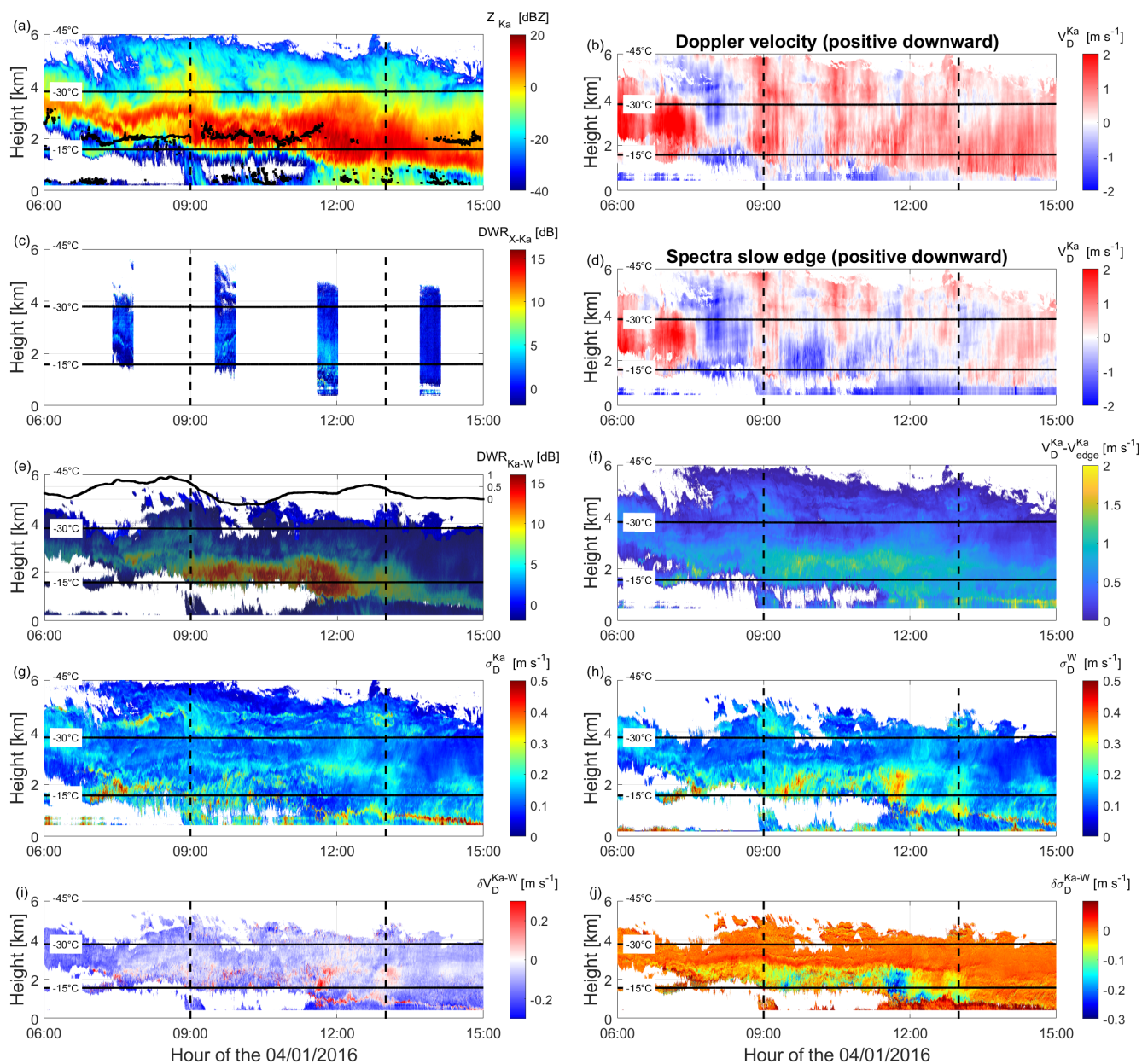
Figure 4. Time height cross section of the (a) KAZR reflectivity, (b) KAZR Doppler velocity V_D^{Ka}, (c) DWR$_{X,Ka}$, (d) Doppler velocity of KAZR spectra slow edge $V_{D,slowedge}^{Ka}$, (e) DWR$_{Ka,W}$, (f) difference between KAZR Doppler velocity and Doppler spectra slow edge $V_D^{Ka} - V_{D,slowedge}^{Ka}$, (g) KAZR spectral width σ_D^{Ka}, (h) MWACR spectral width σ_D^W, (i) differential Doppler velocity between KAZR and MWACR $\delta V_D^{Ka,W}$ and (j) differential spectral width between KAZR and MWCAR $\delta\sigma_D^{Ka,W}$. The horizontal black lines indicate the -15 and -30°C levels while the vertical dashed lines delimit the period of large DWR$_{Ka,W}$ used to produce the density plots in Fig. 5, 6 and 7. The black dots in (a) show the liquid water as detected by the ARM high spectral resolution lidar (HSRL) cloud base height product (Silber et al., 2018a); see also the inset in Fig. 10a. The thick black curve in the upper part of (e) is the 2-way ΔPIA in dB (scale along the right axis) derived from Rayleigh scattering hydrometeors at cloud top (non-shaded zones) following Tridon et al. (2020).

with its own scale on the right axis in dB). While in general, ΔPIA can be due to thick layers of supercooled liquid droplets or dense snow, the ice crystals in this case study are not expected to produce any significant attenuation. ΔPIA can then be used to roughly estimate the supercooled liquid water path within this cloud (Tridon et al., 2020). Before 7:00 UTC and after

185 14:00 UTC, ΔPIA is very close to 0 dB suggesting that ice water path (IWP) and liquid water path (LWP) are small and do not produce any detectable differential attenuation. During the period with largest $DWR_{Ka,W}$ (between 10:00 and 12:00 UTC), ΔPIA reaches 0.25 dB. Assuming that only the supercooled liquid water contributes to the ΔPIA, the corresponding LWP should be of the order of 100 $g\ m^{-2}$, according to recent refracting index models (Tridon et al., 2020). Note that ΔPIA becomes slightly negative (-0.25 dB) between 9:30 and 10:30 UTC. This may be linked to the light snow shower reaching the

190 ground around 9:00 UTC, and be explained by snow accumulating preferentially on the KAZR large flat radome. If this effect persists over the following hours, the true ΔPIA between 10:00 and 12 UTC could be at most 0.5 dB, corresponding to a LWP of the order of 200 $g\ m^{-2}$.

In the upper part of the cloud (4 to 6 km AGL) where the temperature is comprised between -25 and -40°C, the reflectivity and DWRs remain low. As aggregation in this temperature regime can be expected to be relatively weak, we expect plate-like

195 particles and possibly polycrystals to dominate. Closer to the supercooled liquid layer, the $DWR_{X,Ka}$ is found only slightly enhanced (up to 5 dB, Fig. 4c) while the $DWR_{Ka,W}$ reaches the rather extreme value of 15 dB (Fig. 4e), i.e. the largest values in the AWARE field campaign data depicted in Fig. 1a. At temperatures lower than -15°C, aggregation is still expected to be limited and it is unlikely to be the process which leads to very large $DWR_{Ka,W}$ since $DWR_{X,Ka}$ would be also more strongly enhanced if the 15 dB were due to large aggregates. Conversely, such DWR combination strongly suggests an intense

200 riming event, but this assumption cannot be readily corroborated by Doppler velocity because the entire period is affected by significant vertical motions.

The KAZR Doppler velocity, V_D^{Ka} (positive when downward in our convention), is the result of the vertical air motion and the ice particle fall speed. For many instances of the case study, it features periods with negative values (Fig. 4b), i.e. updrafts. These updrafts are even more evident when exploiting KAZR Doppler spectra: the Doppler velocity of the slow edge of the

205 spectra $V_{D,slowedge}^{Ka}$ (i.e., the vertical velocity of the smallest hydrometeors detected in the sampling volume) is practically always negative (i.e. upward), and in some regions by almost 2 $\mathrm{m\,s^{-1}}$ (Fig. 4d).

In case of low turbulence broadening such as in most of this case (Fig. 4g; further discussed in the following paragraph), subtracting the slow edge Doppler velocity from the Doppler velocity $V_D^{Ka} - V_{D,slowedge}^{Ka}$ provides a lower limit for the reflectivity weighted mean fall velocity, or in other words, the Doppler velocity corrected from vertical air motion (Fig. 4f). This

210 subtraction provides a lower boundary because the smallest hydrometeors detected by the radar may not have a negligible fall speed, an issue which will be exacerbated in regions of low radar sensitivity. In such instances, the actual updraft and, consequently, the derived mean fall velocity would both be underestimated. Conversely, enhanced level of turbulence would cause an overestimation of the updraft and of the mean fall velocity. Panels Fig. 4b and d (V_D^{Ka} and $V_{D,slowedge}^{Ka}$) clearly show vertical stripes typically associated with abrupt changes of vertical air motions. Conversely, in panel Fig. 4f ($V_D^{Ka} - V_{D,slowedge}^{Ka}$)

215 the velocity increases downward as expected for ice particles growing via deposition, riming or aggregation while they fall through a cloud, suggesting that most of the variability induced by the vertical air motions has been correctly eliminated. The
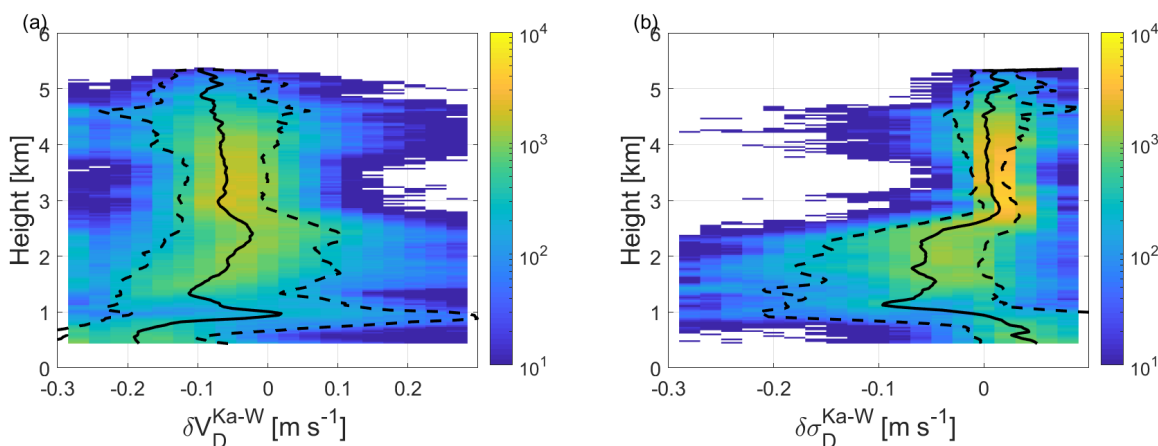
Figure 5. Contoured frequency by altitude diagram of the differential fall velocity $\delta V_D^{Ka,W}$ and differential spectral width $\delta \sigma_D^{Ka,W}$ between KAZR and MWACR during the period of high $DWR_{Ka,W}$ in between the vertical dash lines in Fig.4i and j. The continuous and dashed black lines show the profiles of median, 10th and 90th percentiles of the distributions.

fall velocity of unrimed aggregates is known to be capped at around $1 \, \mathrm{m\,s^{-1}}$, independent of their size because the increase of mass via aggregation is compensated by the enhanced drag due to the larger cross sectional area (Zawadzki et al., 2001; Kneifel and Moisseev, 2020). With values often reaching $1.4 \, \mathrm{m\,s^{-1}}$ between 1.8 and $3 \, \mathrm{km}$ AGL (Fig. 4f), the resulting mean fall velocity supports the presence of at least slightly rimed ice particles.

220   Less directly, the spectral width σ_D can be used to infer some information on ice properties as well (Maahn and Löhnert, 2017). The challenge is to separate the broadening due to the spread of hydrometeor fall velocities from the broadening due to air motion. For a vertically pointing cloud radar, the air motion broadening is mainly due to turbulence, wind shear and cross wind within the scattering volume (Borque et al., 2016). During this case study, the spectrum widths observed by the KAZR

225   (Fig. 4g) is mostly limited to rather small values compatible with the narrow spread of ice crystals fall velocity while only few layers with larger values are probably associated to gravity waves. Since the KAZR and the MWACR have practically identical beam widths (0.33 and 0.36°, respectively) and range resolutions, were the air motion broadening dominating the spectral width, the latter should be identical for both radars. Any difference must therefore be related to the spread of hydrometeors fall velocity and to differential non-Rayleigh effects associated to the large ice crystal PSD tail. Interestingly, the MWACR spectral

230   width is significantly larger than KAZR spectral width in the large $DWR_{Ka,W}$ region (Fig. 4h), which leads to a negative differential spectral width between Ka and W bands $\delta \sigma_D^{Ka,W}$ (Fig. 4j). While the spectral width is generally larger at Ka-band, such a peculiar behaviour is possible for narrow size distributions of large ice crystals, as will be seen in Sect. 4.4.

In order to verify that the negative $\delta \sigma_D^{Ka,W}$ is not a spurious signal due to a possible mismatch of the radar beams, two-dimensional histograms (contoured frequency by altitude diagram, CFAD) of the differential Doppler velocity ($\delta V_D^{Ka,W}$) and

235    $\delta \sigma_D^{Ka,W}$ for the period with high $DWR_{Ka,W}$ are shown in Fig. 5. Above $3 \, \mathrm{km}$ AGL, reflectivity, DWRs, and fall velocity are

small (Fig. 4) suggesting that mostly small ice particles, thus Rayleigh scatterers, are present. In this case, both $\delta V_D^{Ka,W}$ and $\delta\sigma_D^{Ka,W}$ should be very close to zero. When non-Rayleigh targets are present, the Doppler velocity (still with a positive when downward convention) is generally smaller at the higher radar frequency because scattering effects reduce the backscatter cross section of the largest and faster falling ice crystals. The slightly negative $\delta V_D^{Ka,W}$ (-0.5 m s^{-1}) — and hence larger V_D^W —

240 can only be explained by one of the radars slightly pointing off-zenith, as was found for the BAECC dataset (Kneifel et al., 2016). As a result, a small component of the horizontal winds is found along the pointing direction of the mis-pointing radar which explains the observed $\delta V_D^{Ka,W}$ difference. Conversely, being defined as the spread around the mean Doppler velocity, the spectral width is not affected by a bias in Doppler velocity. As expected, $\delta\sigma_D^{Ka,W}$ is centered around zero for the small ice crystals present above 4 km AGL, confirming that the negative $\delta\sigma_D^{Ka,W}$ below 3 km AGL is not an artefact due to mispointing

245 radar beams.

4.3   Evidence of narrow particle size distribution

The reflectivity observed by the three radars within the period delimited by the dashed lines in Fig. 4 are combined in the so-called triple-frequency space (Fig. 6). The bullseye cluster centered around 0-0 dB corresponds to the upper part of the cloud (above 4 km) where the ice particles are small and nearly scatter in the Rayleigh regime at all frequencies. The cluster

250 on the right hand side corresponds to the lower part of the cloud where supercooled liquid water is present. The combination of very high DWR$_{Ka,W}$ and rather small DWR$_{X,Ka}$ is known to be the signature of rimed aggregates. In this case, this riming signature appears much stronger than previously observed (Kneifel et al., 2015; Mason et al., 2018; Dias Neto et al., 2019).

For reference, the lines superimposed in Fig. 6 show DWRs of exponential distributions of unrimed and rimed ice crystals forward modelled using various scattering models designated as electromagnetic-microphysical (hereafter EM-MIC) models

255 following the nomenclature introduced in Tridon et al. (2019). Light gray to dark gray lines correspond to the self-similar Rayleigh-Gans approximation (Hogan and Westbrook, 2014; Hogan et al., 2017) for realistic ensembles of ice aggregates (B model of Leinonen and Szyrmer, 2015) with various degrees of riming (from unrimed SSRGA-LS15-B0kgm2 to heavily rimed SSRGA-LS15-B2kgm2). Blue, purple and red lines correspond to T-matrix scattering calculations for oblate spheroid ice crystals with an axial ratio of 0.6 and composed of a homogeneous ice-air mixture (soft spheroid model). The different lines

260 correspond to various densities which are determined from the density factor r introduced by Mason et al. (2018) (from unrimed TMAT-M18-r0 when $r = 0$ to nearly hail TMAT-M18-r0.8 when $r = 0.8$). Fig. 6 clearly shows that none of the scattering models corresponding to rimed particles can explain the observed reflectivities, if exponential distributions are assumed.

Mason et al. (2019) showed that the shape of the ice particle size distribution (PSD) can also affect the triple-frequency radar signature: reducing the width of a PSD (e.g. by increasing the shape parameter μ of a gamma PSD) has a similar effect to that

265 of increasing the particle density. As a result and since riming has been shown to be correlated with narrow size distributions (Garrett et al., 2015), a narrow PSD could amplify the triple frequency signature of riming and is the most plausible way to explain the extreme signature observed in this case.
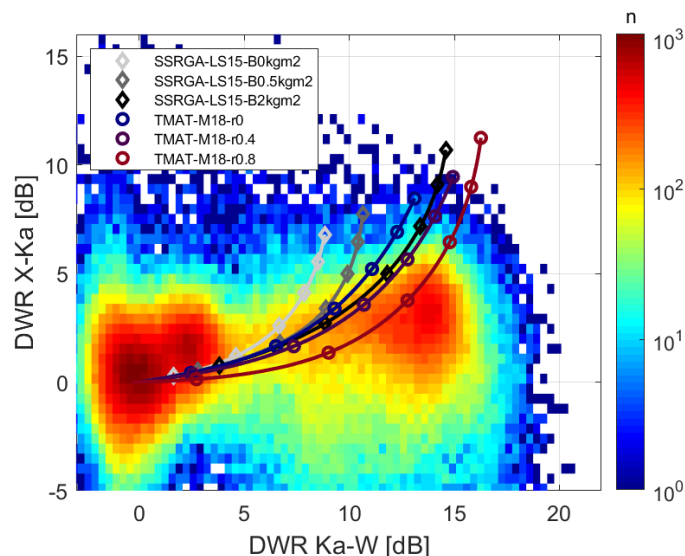
Figure 6. Joint histogram of measured dual-wavelength ratios (DWRs) for triple-frequency radar observations. Superimposed curves represent the forward modeled DWR for an exponential distribution of particles with a mean mass diameter comprised between $0 < D_m \leq 6\,\mathrm{mm}$ (each marker corresponding to $1\,\mathrm{mm}$ step) using various electromagnetic-microphysical models (see details in the text).

4.4 Constraining ice particle properties from multi-frequency radar observations

In order to take into account the effect of the shape of the PSD, we consider gamma distributions of the form:

$$N(D) = N_0^* f(\mu)(D/D_m)^\mu \exp^{-\Lambda D} \tag{1}$$

where Λ and μ are the slope and shape parameters, $D_m = (1 + \mu + b_m)/\Lambda$ is the mean mass diameter, b_m is the exponent of the mass-size relation associated to the EM-MIC model and $f(\mu)$ is a normalisation factor following Testud et al. (2001). In comparison to an exponential distribution, a gamma distribution (with μ larger than zero) leads to larger $\mathrm{DWR}_{Ka,W}$ for any EM-MIC model (Mason et al., 2019, and Fig. 7a). However, it also leads to a reduced spectral width and, as was shown in Sect. 4.2, the observed negative $\delta\sigma_D^{Ka,W}$ is a very specific feature and is an evidence that the PSD is wide enough to contribute to the spectral width. Therefore, combining the triple-frequency radar signature with the observed σ_Ds offers a way to constrain the best EM-MIC model matching the observations (e.g., by comparing the density plots of these observations as function the $\mathrm{DWR}_{Ka,W}$ to the theoretical lines provided by the EM-MIC models). Furthermore, even if the estimation of $V_D - V_{D,slowedge}$ requires a negligible turbulence broadening and a high radar sensitivity, Sect. 4.2 and Fig. 4 suggest that these conditions are reasonably fulfilled for this case study. Then, since the $V_D - V_{D,slowedge}$ parameter is unaffected by the vertical wind, it is a further parameter that can be used to evaluate EM-MIC models, contrary to the Doppler velocity. To this aim, Doppler spectra with a realistic noise level are simulated following the methodology described in Tridon and Battaglia (2015) and $v_{D,slowedge}$

is determined as being the Doppler velocity of the first bin with spectral reflectivity larger than the noise, as for the observed Doppler spectra.

285   The resulting density plots of observations are shown in Fig. 7, in which the superimposed theoretical lines correspond to a new EM-MIC model briefly introduced below. By using a similar methodology, Fig. S1 and Fig. S2 of the supplementary material provide an assessment on how well the two types of rimed aggregates EM-MIC models discussed in the previous section (i.e. SSRGA-LS15-B1kgm2 and TMAT-M18-r0.4) fit the radar observations. Interestingly, despite choosing the most adequate degree of riming, these models appear to be inconsistent with the measurements for the following reasons:

290   – For the SSRGA-LS15 type (Fig. S1), a rather high degree of riming (equivalent liquid water path of 1 kg m^{-2}) is required to produce large enough $DWR_{Ka,W}$. This is very surprising because this EM-MIC model corresponds to heavily rimed particles while the small ΔPIA between Ka and W-bands (see Sect. 4.2) suggests that the amount of observed supercooled liquid water is relatively small. This leads to excessive simulated fall velocities and spectral widths, with particularly high $V_D^{Ka} - V_{D,slowedge}^{Ka}$ at small $DWR_{Ka,W}$, resulting in a completely inadequate sloping of this parameter

295   with increasing $DWR_{Ka,W}$.

    – A much better agreement is found for the TMAT-M18 type when using a density factor r=0.4 and shape parameter $\mu = 4$ (Fig. S2). Nevertheless, the resulting $V_D^{Ka} - V_{D,slowedge}^{Ka}$ and σ_D^{Ka} are slightly too large. Furthermore, this model appears less physical since it suggests that very high $DWR_{Ka,W}$ (larger than 20 dB) could be reached in case of very narrow size distributions ($\mu \geq 16$), while the observations suggest a clear cut-off above 15 dB.

300   Note that the Doppler velocity comparison is not without uncertainty: first, the proposed vertical air motion correction is an approximation; and second, the hydrodynamic theory for ice particles of complex shape is still a topic of active research, with the different hydrodynamic models proposed in the literature (Böhm, 1992; Khvorostyanov and Curry, 2005; Heymsfield and Westbrook, 2010) known to lead to slightly different fall velocities (different line widths in Fig. 7b). Nevertheless, this uncertainty is much smaller than the large overestimation found with the SSRGA-LS15-B1kgm2 model.

305   A possible explanation for the excessive Doppler velocities of the SSRGA-LS15-B1kgm2 models could be in its mass-size relation. Indeed, the mass-size relation parameters of the Leinonen and Szyrmer (2015) B model for heavily rimed particles are quite different from those derived from various observations according to the comprehensive review made by Mason et al. (2018, their Fig. 1). The rather large prefactor with low exponent lead to particularly large masses for corresponding sizes. While the aggregation and riming model used in Leinonen and Szyrmer (2015) is widely accepted and provides physically

310 reasonable particle shapes (Seifert et al., 2019; Karrer et al., 2020), it remains debatable how realistic it is to cluster the ice particles by the equivalent LWP of supercooled droplets through which they sediment. This model indeed assumes an ideal seeder-feeder cloud situation with the same riming efficiency at all ice particles sizes.

    Instead, we propose to cluster rimed particles according to their normalized rime mass, $\mathcal{M}$, defined by Seifert et al. (2019) as the ratio of the particle mass m to the mass m_g of a 700 kg m^{-3} graupel of equivalent size. Such parameter is better suited

315 to represent successive stages of riming since its definition literally translates the asymptotic increase of m toward m_g, and it allowed Seifert et al. (2019) to illustrate the self-similarity of the conversion of aggregates to graupel-like particle. In order to
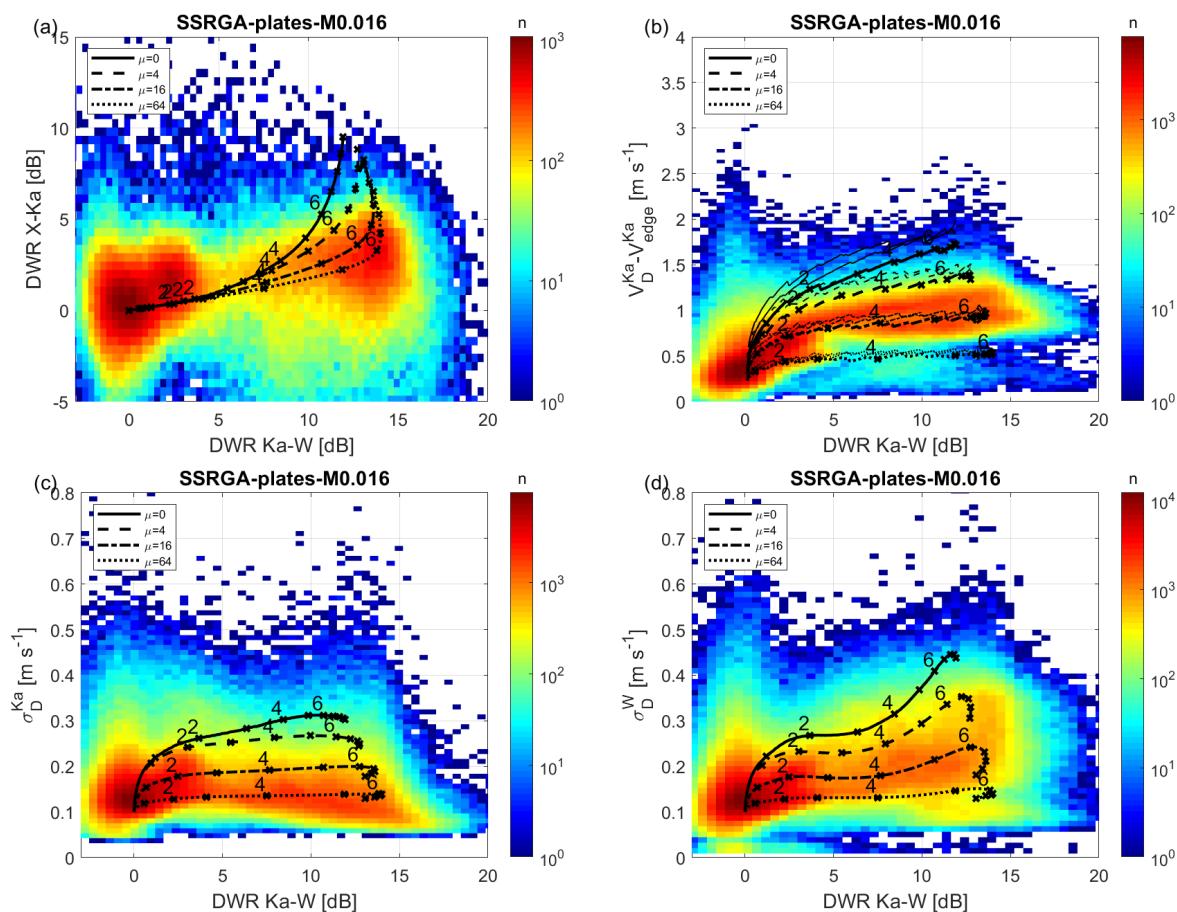
Figure 7. Joint histogram of observed (a) $\text{DWR}_{X,Ka}$, (b) difference between Ka-band Doppler velocity and Doppler spectra slow edge $V_D^{Ka} - V_{D,slowedge}^{Ka}$, (c) Ka-band spectral width σ_D^{Ka} and (d) W-band spectral width σ_D^W as function of observed $\text{DWR}_{Ka,W}$. Superimposed lines represent the corresponding parameters forward modeled with the SSRGA for a gamma distribution of aggregates of plates with various μ (see the legends in the plots), a mean mass diameter comprised between $0 < D_m \leq 10$ mm (each marker corresponding to 1 mm step) and a normalized rimed mass $\mathcal{M} = 0.016$ (see the text for details). In panel (b), thick lines correspond to calculations of fall velocities using the Böhm (1992) model while thin lines correspond to the Khvorostyanov and Curry (2005) and Heymsfield and Westbrook (2010) models.

Table 2. Parameters of the main EM-MIC models used in this study: mass-size relation parameters (prefactor a_m and exponent b_m), effective aspect ratio (α_{eff}) and SSRGA parameters (kurtosis parameter κ, power-law prefactor β and exponent γ, and correction factor ζ_1) averaged over the 1-10 mm range of sizes. To obtain the parameters of the other EM-MIC models of Fig. 6, the reader can refer to Leinonen and Szyrmer (2015) and Mason et al. (2018) for the SSRGA-LS15 and TMAT-M18 series, respectively.

EM-MIC model	a_m	b_m	α_{eff}	$\overline{\kappa}$	$\overline{\beta}$	$\overline{\gamma}$	$\overline{\zeta_1}$
TMAT-M18-r0.4	0.68	2.34	0.6	N/A	N/A	N/A	N/A
SSRGA-LS15-B1kgm2	0.37	2.11	0.79	0.17	2.55	3.34	0.06
SSRGA-plates-$\mathcal{M}0.016$	0.52	2.43	0.53	0.26	2.05	2.57	0.07

build new EM-MIC models corresponding to specific $\mathcal{M}$ values, we used the open code provided by Leinonen and Szyrmer (2015) and produced an ensemble of rimed aggregates with a wide range of $\mathcal{M}$ (leading to more diversified degrees of riming than what was proposed in Leinonen and Szyrmer, 2015). Since the DWRs observed during the case study start to increase in
320 the plate-like growth regime, plate aggregates or polycrystals are quite likely and we chose plates as primary ice crystal shape for the simulations. We then used the Snowscatt tool (Ori et al., 2020) to derive the SSRGA parameters for various $\mathcal{M}$ classes. While the full discussion of the resulting rime ice particle classes is beyond the scope of this study and will be fully described in a subsequent paper, the resulting $\mathcal{M}$ classes provide mass-size parameters which are significantly different from previous studies, but are consistently increasing (not shown) in agreement with riming theory, in particular, with an exponent increasing
325 from 2 (fractal geometry of unrimed aggregates) to 3 (spherical particles, i.e. fully rimed). Especially, for corresponding sizes, these mass-size parameters lead to smaller masses and fall velocities than the Leinonen and Szyrmer (2015) B model. With a normalized rimed mass $\mathcal{M} = 0.016$ and a μ value on the order of 16, the resulting slightly rimed particle class provides a reasonable agreement with the observed triple-frequency DWRs, spectral widths, and fall velocity, all at the same time (Fig. 7). In this scenario, the high $DWR_{Ka,W}$ cluster in Fig. 7a corresponds to mean mass diameter D_m ranging from 5 to 7 mm.
330 For comparison, the parameters of the SSRGA-plates-$\mathcal{M}0.016$ model are compared to those of previous EM-MIC models in the Table 2. Apart from the mass-size parameters, a significant difference resides in the effective aspect ratio (α_{eff}): for the SSRGA-LS15-B1kgm2 model, it is closer to unity suggesting rounded particles and heavy riming, while SSRGA-plates-$\mathcal{M}0.016$ has a value closer to 0.6, the value widely accepted in the literature and more consistent with slight riming.

4.5 Retrieval of ice properties

335 In order to constrain the ice particle properties from multi-frequency radar observations, numerous assumptions are required. The most important one is the EM-MIC model (and its associated mass-size relation) chosen to describe the type of ice particles. In an effort to evaluate the uncertainty associated with this choice, a simple retrieval of ice properties using the multi-frequency radar data and the most likely ice particle types is proposed in this section.

The retrieval assumes an EM-MIC model and is applied for each ice particle type independently. Its aim is to retrieve
340 parameters such as ice particle number concentration n_i, ice water content (IWC) and mean mass diameter D_m. To do so, it

is required to invert the ice particle size distribution (PSD). By assuming a gamma PSD (Eq. (1)), three parameters must be retrieved: N_0^*, μ and D_m. The core of the methodology is to retrieve μ and D_m via a simple minimization technique (such as in Turk et al., 2011) and its main steps are as follows:

1. For each EM-MIC candidate, we build a multidimensional lookup table that provides the forward simulated $DWR_{X,Ka}^{sim}$, $DWR_{Ka,W}^{sim}$ and $V_D^{sim} - V_{D,slowedge}^{sim}$ at the Ka band (where the Ka subscript is omitted for simplicity) corresponding to any $\mu - D_m$ pair.

2. For each combination of measurements, $DWR_{X,Ka}^{obs}$, $DWR_{Ka,W}^{obs}$ and $V_D^{obs} - V_{D,slowedge}^{obs}$, the best matching $\mu - D_m$ pair is found by minimizing the cost function CF:

$$CF = \frac{\left|DWR_{X,Ka}^{obs} - DWR_{X,Ka}^{sim}\right|}{\sigma_{DWR_{X,Ka}}} + \frac{\left|DWR_{Ka,W}^{obs} - DWR_{Ka,W}^{sim}\right|}{\sigma_{DWR_{Ka,W}}} + \frac{\left|(V_D^{obs} - V_{D,slowedge}^{obs}) - (V_D^{sim} - V_{D,slowedge}^{sim})\right|}{\sigma_{V_D - V_{D,slowedge}}}, \quad (2)$$

where $\sigma_{DWR_{X,Ka}}$, $\sigma_{DWR_{Ka,W}}$ and $\sigma_{V_D-V_{D,slowedge}}$ are the measurements errors corresponding to those observations. Based on the joint histograms of Fig. 7, these errors have been set to 3 dB, 1.5 dB and 0.2 m s^{-1}, respectively. This provides a direct mapping from a set of measurements $DWR_{X,Ka}^{sim}$, $DWR_{Ka,W}^{sim}$ and $V_D^{sim} - V_{D,slowedge}^{sim}$ to the unknowns $\mu - D_m$.

3. The mapping from the measurements to the unknowns is highly non-linear. The error associated to this variability is taken into account via Monte Carlo propagation. Namely, the retrieval is performed several times on an ensemble obtained by perturbing each measurement via normally distributed measurement errors with standard deviations $\sigma_{DWR_{X,Ka}}$, $\sigma_{DWR_{Ka,W}}$ and $\sigma_{V_D-V_{D,slowedge}}$, respectively. For each set of measurements, a $\mu - D_m$ pair is retrieved and the resulting retrieval errors σ_μ and σ_{D_m} are obtained by taking the standard deviation of the ensemble of retrieved μ and D_m values.

4. Once μ and D_m and their uncertainty are retrieved for a data voxel, N_0^* can be directly derived from the observed reflectivity Z_{Ka} thanks to the relation

$$N_0^* = \frac{\pi^5 |K|^2}{\lambda_{Ka}^4} \frac{Z_{Ka}}{\int \sigma_b^{\text{EM-MIC}}(D) D^\mu \exp^{-\Lambda D} dD}, \quad (3)$$

while its standard deviation $\sigma_{N_0^*}$ is computed via error propagation, assuming that σ_μ and σ_{D_m} are independent.

5. Finally, IWC and ice number concentration n_i and their errors are computed using:

$$n_i = N_0^* \int D^\mu \exp^{-\Lambda D} dD, \quad (4)$$

$$IWC = N_0^* \int a_m D^{b_m} D^\mu \exp^{-\Lambda D} dD, \quad (5)$$

where a_m and b_m are the prefactor and exponent of the mass-size relation associated to the EM-MIC model.

The retrieval is applied with the three EM-MIC models, which were found to better describe the joint histograms of observations in Fig. 7, Fig. S1 and Fig. S2: SSRGA-plates-$\mathcal{M}$0.016, SSRGA-LS15-B1kgm2 and TMAT-M18-r0.4. As an example,
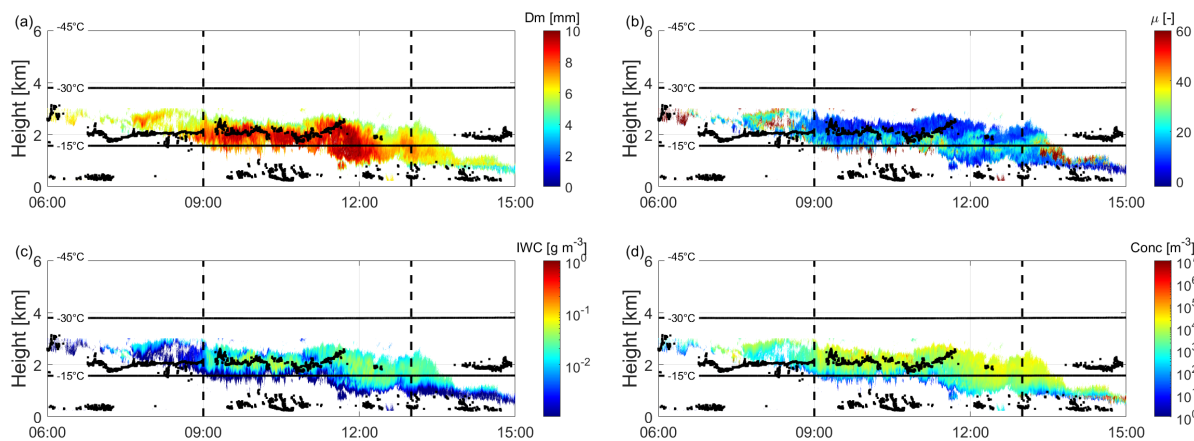
Figure 8. Time height cross section of the retrieved (a) D_m, (b) μ, (c) IWC and (d) N_i when using the SSRGA-plates-$\mathcal{M}0.016$ model, for all pixels where $\mathrm{DWR}_{Ka,W}$ is larger than 4 dB. The black dots show the location of supercooled liquid water as detected by the ARM high spectral resolution lidar.

Fig. 8 illustrates the results of the retrieval using the SSRGA-plates-$\mathcal{M}0.016$ model. For simplicity, it is applied only to the data identified as rimed by requiring the $\mathrm{DWR}_{Ka,W}$ to be larger than 4 dB (of course, such a simple threshold is valid for this particular case study only because aggregation is negligible in the unrimed part of the cloud). Apart from μ, which appears slightly noisy, the retrieved fields are reasonably homogeneous. At the top of the layer, a strong increase of D_m towards the ground is seen, which could be linked to the supercooled liquid layer. From 2 km AGL downward, there is a clear decrease of n_i and IWC, consistent with sublimation of snow when it mixes with dry air in the boundary layer.

The fields of parameters retrieved with SSRGA-LS15-B1kgm2 and TMAT-M18-r0.4 (not shown) are similarly homogeneous as for SSRGA-plates-$\mathcal{M}0.016$. However, significant and consistent differences are found throughout the entire case study. For simplicity, the retrieved parameters are compared in Fig. 9 for a single profile at 11:58:09 UTC where the $\mathrm{DWR}_{Ka,W}$ is maximum, but the results are similar for all other profiles. While all three EM-MIC models agree fairly well on the retrieved μ values peaking at 20 between 1.4 and 2.2 km AGL, the range of D_m values is not very well constrained owing to the discrepancies between the EM-MIC model attributes (Table 2): SSRGA-plates-$\mathcal{M}0.016$ suggests D_m values about twice as large as SSRGA-LS15-B1kgm2. Sensitivity tests (not shown) indicate that this large difference is mainly due to the unexpectedly high aspect ratio associated with the SSRGA-LS15-B1kgm2 model. With a smaller and more realistic aspect ratio, the particles of the SSRGA-plates-$\mathcal{M}0.016$ model have a shorter dimension along the scattering direction, resulting in lesser destructive interferences at higher radar frequencies, a weaker reduction of the backscatter cross section of large particles, and hence, smaller DWRs for corresponding sizes. With TMAT-M18-r0.4, this effect is cancelled by the distinct method used for the scattering calculations and the resulting D_m are close to those of SSRGA-LS15-B1kgm2 by coincidence. In a nutshell, the resulting uncertainty on D_m is large because the particle shape is under-constrained. We can only conclude with confidence that the par-
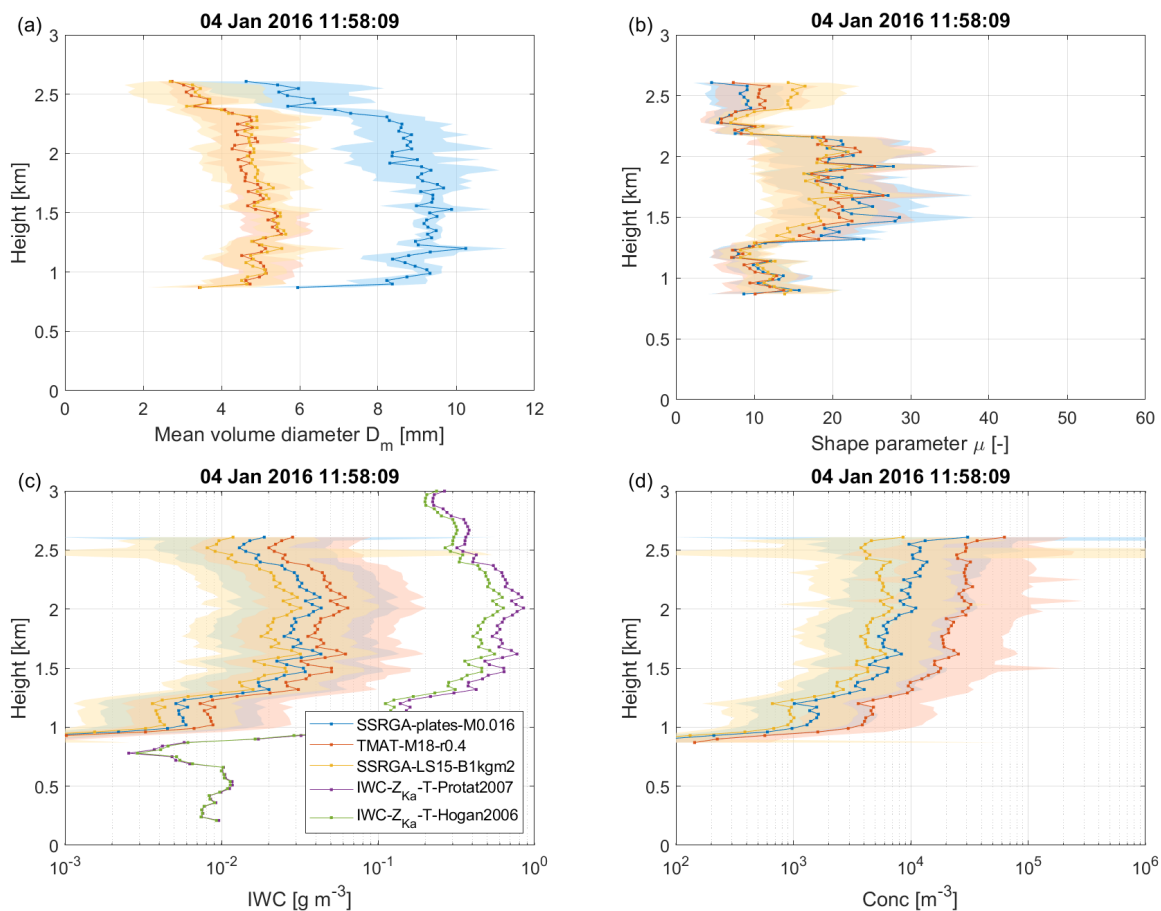
Figure 9. Comparison of (a) D_m, (b) μ, (c) IWC and (d) n_i profiles at 11:58:09 UTC retrieved with the most probable EM-MIC models identified in Sect. 4.4. Colored shadings show the corresponding ± 1 standard deviation.

ticles are notably large, with a D_m on the order of 4 mm or larger. Furthermore, knowing that both the SSRGA-plates-$\mathcal{M}0.016$ and SSRGA-LS15-B1kgm2 models have been derived from the same aggregation and riming model, additional work is needed

390   to determine which aspect ratio is the most realistic and to be able to derive D_m with a better accuracy. Interestingly, n_i and IWC retrieved with the three different EM-MIC models are in a fairly good agreement despite the large difference in D_m, which suggests that these parameters are rather well constrained when combining reflectivity observed at X, Ka and W-bands and the $V_D^{sim} - V_{D,slowedge}^{sim}$ estimate.

    Likewise, the figure 9c also shows the IWC retrieved using the climatological IWC-Z_{Ka}-T relationships of Hogan et al.

395   (2006) and Protat et al. (2007, for midlatitude). They result in IWCs more than one order of magnitude larger than the EM-MIC models suggesting that such simple statistical relations are not suited for specific conditions like the narrow size distributions of this case.

In summary, despite the lack of in situ observations for constraining the ice particles properties, the detailed exploitation of triple-frequency radar observations allowed us to conclude that the specific radar signature observed during this case study was

400   due to narrow distributions of large and slightly rimed plate polycrystals. It the next section, we devise a bin model experiment to better understand whether riming and such a narrow PSD can be physically consistent.

4.6   Bin model experiment: can the observed narrow PSD of rimed ice particles be reproduced?

4.6.1   Model setup and initialization

To examine whether a plausible riming scenario could develop the triple-frequency signature detected in the observations, we

405   use the Distributed Hydrodynamic Aerosol and Radiative Modeling Application (DHARMA) model (Stevens et al., 2002) coupled with the Community Aerosol-Radiation-Microphysics Application (CARMA) size-resolved bin microphysics model (Ackerman et al., 1995; Jensen et al., 1998). Our main hypothesis in this modeling exercise is that the high μ values suggested by the observations are most likely to occur if the ice hydrometeors dominating the radar echoes originate from a shallow generating layer and experience little to no mixing before the combined $DWR_{X,Ka}$ and $DWR_{Ka,W}$ signatures are produced. That

410   is because a deep generating layer or strong mixing of rimed ice hydrometeors would necessarily lead to stronger dispersion of size-dependent ice particle fall velocities at given air volumes and broadening of the ice PSD (lower μ). Such broadening of the PSD implies larger contribution of particle sizes producing lower $DWR_{Ka,W}$ and/or higher $DWR_{X,Ka}$ (Fig. 7) to the total output signatures resulting in deviation from the observed DWR values. This hypothesis is supported by the small spectral width values (Fig. 4g) and the largely stable atmospheric profile during the event indicated by the potential temperature

415   sounding measurements (Fig. 10a).

As indicated by the high spectral resolution lidar (HSRL; Eloranta, 2005) measurements (Fig. 4a and Fig. 10a's inset), a distinct supercooled cloud layer was continuously observed over McMurdo Station at altitudes of 1.7-2.5 km ASL. Nevertheless, the sounding relative humidity (RH) measurements (Fig. 10c) show too low values at these altitudes peaking at 84%. Considering the cloud field extent during the event based on the satellite measurements (figs. 2 and 3), we postulate that even

420   with the radiosonde horizontal drift of a few kilometers away from McMurdo until it reached an altitude of 2.5 km ASL, it could not reach a liquid-free layer. Therefore, we deduce that the radiosonde RH measurements became negatively biased at some point of balloon's flight by up to ∼16%. We note that such negative RH measurement biases were detected in some other cases during AWARE based on HSRL, KAZR, and sounding cross-validation (not shown), and were occasionally occurring at other sites as well. Based on this deduction and supported by indications of a geometrically-thick liquid water hydrometeor

425   population in the KAZR spectra (not shown), we conclude that a deep supercooled layer was extending from about 1.7 to 3.6 km ASL, with a possible break of a few hundred meters centering at ∼2.6 km ASL (Fig. 10c). The location of this deep supercooled layer suggests that even if some vertical mixing did occur during this event (at 3.5-4.2 km ASL and 6.4-6.7 km ASL; see vertical potential temperature profiles in Fig. 10a), it mostly took place at altitudes where the ice particle population did not yet experience rapid mass growth due to high ice supersaturation conditions (Fig. 10d) and/or intense riming. The potentially
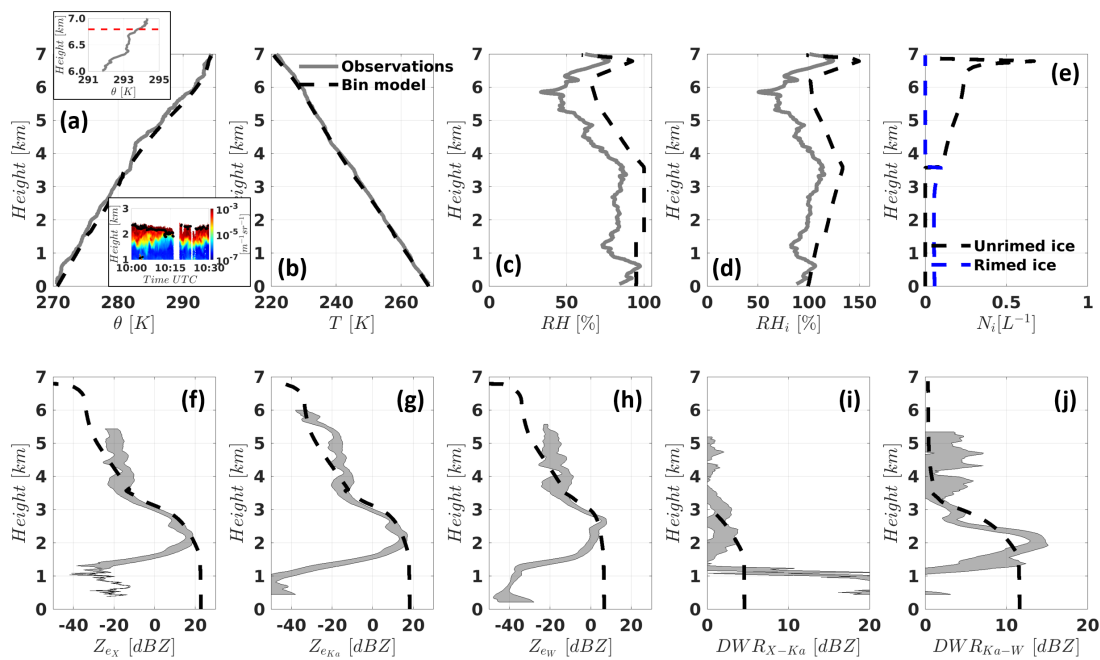
Figure 10. Sounding (10:24 UTC) and radar (09:30-09:55 UTC) measurement profiles together with the bin model output at the end of the 8-h simulation. (a) Potential temperature (θ), (b) temperature, (c) relative humidity (RH), (d) RH with respect to ice (RH_i), (e) unrimed and rimed ice number concentration (model only; see legend), (f) measured temporal mean ±1 standard deviation XSACR (shaded region) plus model forward-calculated X-band (black dashed line) reflectivities, (g) as in panel f but for KAZR (Ka-band), (h) as in panel f but for MWACR (W-band), (i) as in panel f but showing the $DWR_{X,Ka}$, and (j) as in panel f but showing the $DWR_{Ka,W}$. The insets in panel a depict the θ profile between 6 and 7 km ASL altitude with the dashed red line designating the RH peak (see panel c) at 6.8 km ASL (top), and backscatter cross section measured with the HSRL around radiosonde release time together with liquid cloud base heights (black markers; see Silber et al., 2018a, b).

430   mixed layer between the surface and 1.2 km ASL was below the DWR signatures around 2 km ASL examined in this study, and hence, had no impact on the observed signatures.

The sounding RH bias also indicates that it is plausible that the ∼100 m thick RH peak value aloft of 77.5% at 6.7 km ASL was actually greater, on the order of 93-94%. The source of this elevated shallow high-RH layer could be associated with the apparently mixed ∼300 m deep underlying layer potentially transporting relatively warmer and moister air aloft (Fig. 10a and

435   its inset). However, a detailed investigation of this moisture source as well as the generating mechanism of the elevated mixed layer, which could be related to gravity wave breaking, for example (e.g., Lane and Sharman, 2006; Podglajen et al., 2017), is beyond the scope of this study.

The inferred RH peak-values (>90%) in this elevated layer suggest that homogeneous freezing of humidified aerosols (here-after aerosol freezing; e.g., Jensen and Ackerman, 2006; Jensen et al., 2001) might have played a role in the initial formation

440   of at least some of the ice population examined in this study, owing to the large RH_i values (Fig. 10d), which occurred close
to water saturation at a low temperature of -50°C measured at the RH-peak altitude (Fig. 10b). Continuous precipitation of ice
from an altitude of ∼7 km ASL is indicated by spaceborne radar echoes over the region (Fig. 2) as well as by the ground-based
radar echoes (below ∼6 km ASL; Fig. 4). The difference between the topmost radar echoes in the ground-based versus space-
borne measurements could be the result of relatively small ice particles between 6-7 km ASL (especially if indeed formed via

445   aerosol freezing) combined with the limited ground-based radar detectability at the upper troposphere (e.g., Silber et al., 2021).

   Following this discussion while acknowledging that our constraining observations over the depth of the atmospheric profiles
are relatively limited in space and time, we use a simplified approach, where possible, to initialize and run the bin model.
Thus, we run the model over a 1-dimensional (column) domain justified by generally stable atmosphere. We also nudge the
bin model simulation thermodynamically (liquid potential temperature and total water) to the local sounding measurements

450   over McMurdo Station (Figs. 2 and 10) using a nudging time scale of 15 min. That is, because the long duration of the triple-
frequency signature (∼5 h) suggests steady-state Eulerian conditions. Moreover, the highly-complex flow fields typical to the
McMurdo region (e.g., Silber et al., 2019a, Fig. S1) often result in large reanalysis and regional model biases in reproducing
local flow patterns and thermodynamic fields (see Silber et al., 2019b), inhibiting the option of faithfully informing the Eulerian
column model with advective tendencies. With the implemented 15-min nudging time scale, our 8-h long sensitivity test

455   simulations typically reach steady state after 3-5 h, allowing us to process and examine the bin model output profiles at the end
of the simulation.

   Our simplified approach is also incorporated in our treatment of the initialized (and nudged) thermodynamic profile as well
as in the treatment of ice nucleation. Ice nucleation is represented only via homogeneous freezing of humidified ammonium
bisulfate aerosol or activated droplets (heterogeneous ice nucleation is neglected). Since only aerosol freezing occurs here,

460   the ice number concentrations are effectively determined by the RH maximum within the most elevated moisture layer. In the
simulation discussed below, which provided rough agreement with observations, the model is being nudged to an RH peak
value of 94%, consistent with the RH bias discussion above. We note that results similar to the examined simulation at the
bottom 3.5 km ASL were also obtained in different model simulations (not shown) in which ice nucleation via heterogeneous
immersion freezing was included and presented the only source of ice crystals (without aerosol homogeneous freezing aloft,

465   thus omitting the mid-to-upper tropospheric ice); in that case, ice nucleation was concentrated at ∼3.6 km ASL, at the top of
the deep supercooled layer.

   The RH profile below the moisture layer peak is set such that the full profile is supersaturated with respect to ice (Fig. 10d),
thereby excluding potential ice sublimation and growth convolution effects on the model output. The RH profile is set to be
supersaturated between ∼1.7-3.6 km ASL (Fig. 10c), enabling the formation and persistence of the deep supercooled layer in

470   steady-state. The sounding temperature measurement profile is kept unmodified (Fig. 10). Aerosol are set to a log-normal PSD
with a mean diameter of 0.076 μm, a geometric standard deviation of 1.5, and total concentration of 430 cm^{-3}, the values of
which are based on monthly mean surface measurement at AWARE for January 2016 (Liu et al., 2018).

   The bin model is initialized with a single liquid water group and two ice groups: one for unrimed (pristine) ice and another
for rimed ice. Each hydrometeor group consists of 60 bins with a minimum radius of 1 μm and mass ratio between consecutive

475   bin radii of 1.5, allowing maximum particle diameter of a few centimeters. For the unrimed ice group, we use mass- and area-diameter power law parametrizations for radiating plates taken from Fridlind et al. (2012, Table 1), which generally correspond with the polycrystal ice habit regimes (Bailey and Hallett, 2009) of the generating layer, whether it was actually the elevated moisture layer at ∼6.7 km ASL or at the top of the deep supercooled layer at ∼3.6 km ASL (Fig. 10). The rimed ice mass- and area-diameter power law parametrizations we use are the SSRGA-derived parameters for $\mathcal{M} = 0.016$ discussed in Sect. 4.4.

480   Collision and accretion between droplets (creating larger droplets or drops), between unrimed ice and droplets (converting to rimed ice), and between rimed ice and droplets (increasing rimed ice mass) are computed from pairwise particle properties (masses, maximum dimensions, aspect ratio, and projected areas) following Böhm (1999, 2004). Aggregation of ice particles is neglected. Consistently, the forward radar calculations are performed using the same SSRGA method informed by the bin model output.

4.6.2   Model results

485   The model simulation reached steady-state conditions after ∼5 h. During steady-state, in-cloud mean droplet number concentration is ∼30 cm^{-3}. The domain's LWP is ∼220 g m^{-2}, in general agreement with rough LWP estimates on the order of 100-200 g m^{-2} using the method developed by Tridon et al. (2020). Ice water path (IWP) retrievals following Hogan et al. (2006) using the sounding temperature and KAZR reflectivity measurements suggest values during the event on the order of

490   400 g m^{-2} (see Fig. 9), the highest IWPs observed during AWARE. The model steady-state IWP values of ∼165 g m^{-2} are in general agreement with these retrievals considering the high uncertainty associated with this (and other) radar-based ice water content retrievals (e.g., Heymsfield et al., 2008).

  Fig. 10 illustrates profiles of ice particle concentrations (panel e) together with forward calculated reflectivities and DWRs (panels f-j) corresponding to the end of simulation (8 h). Initial ice nucleation occurs at the elevated RH layer via aerosol

495   freezing with a maximum ice number concentration of ∼0.7 L^{-1} (Fig. 10e). The ice number concentration apparently decreases with height because the ice particle fall velocities increase with decreasing height as their mass becomes larger due to vapor growth under the ice-supersaturated conditions, reaching roughly uniform concentrations with height that are consistently smaller than retrieved, as discussed further below. As the precipitating ice particles reach an altitude of ∼3.6 km ASL, the ice particles become rimed and quickly gain additional mass.

500   Intensification of the Ka- and X-band reflectivities at these lower altitudes in which the deep supercooled layer exists (Fig. 10f-g; the W-band reflectivity intensification in Fig. 10h is less pronounced) is commensurate with this rapid mass growth. These reflectivity strengthening patterns and values down to the reflectivity peak (between 2.1-3.5 km ASL) are in reasonable agreement with the radar observations. Note that reflectivity aloft is underestimated in this model simulation by up to several dB, which could be attributable to possible biases in the representation of unrimed polycrystals or underestimated ice number

505   concentrations.

  The model-based DWRs within the deep supercooled layer where the triple-frequency signature was detected show key similarities with the observations; that is, the DWR$_{X,Ka}$ is kept at low values (< 5 dB) while the DWR$_{Ka,W}$ increases to large

values of ∼12 dB (Fig. 10i-j). This comparability is also demonstrated in Fig. 11a showing the spread in the observed DWR values at different height ranges together with the temporally-averaged values and the bin model output.
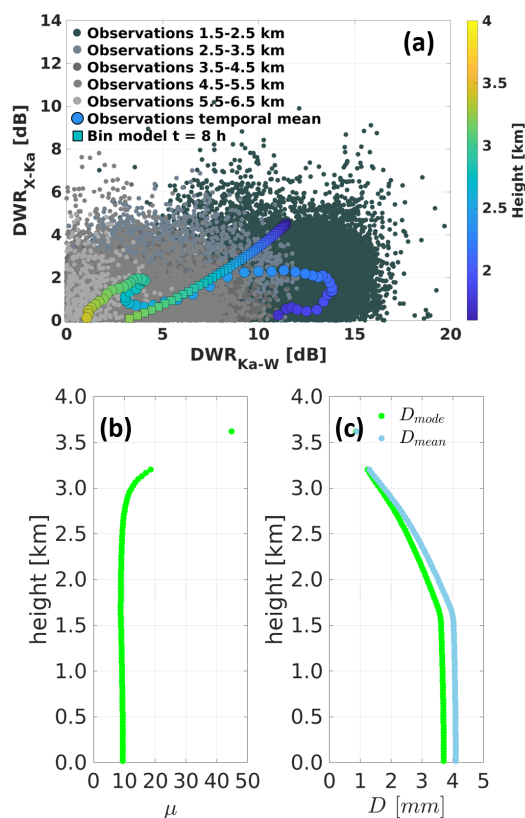
Figure 11. (a) DWR parameter space scatter plot showing the observations (09:30-09:55 UTC) at different height ranges, the temporal-mean observations (color scale denotes height), and the bin model output at the end of the simulation (8 h) (see legend). (b) Shape parameter (μ) derived from gamma distribution fits for the rimed ice group at different heights. μ values are only shown for fits in which the adjusted r^2 is larger than 0.98. (c) Mode and mean diameter of the rimed ice group using the gamma fit parameters under the same adjusted r^2 threshold.

510   To examine the correspondence of this case study's observational analysis conclusions concerning the shape of the ice PSD able to generate the observed triple-frequency signatures (Sect. 4), we perform a gamma distribution fitting to the bin array profile of the rimed ice group at the end of the simulation. Fig. 11b shows a profile of μ derived from gamma distribution fits that agree reasonably well with the rimed ice PSD (adjusted $r^2 > 0.98$). The μ profile indicates a very narrow PSD ($\mu > 40$) at the top of the supercooled layer followed by stabilization of μ values at a range of 9-11 at lower heights, which is consistently

515   lower than the best fit to observations ($\mu \sim 20$). The mean and median ice particle diameters range between 3 and 4 mm over the height range around 2 km ASL corresponding to the DWR signatures (Fig. 11c).

     Taken together, these model results offer general support for the observational and theoretical analysis of the triple-frequency signatures detected during this January 4 2016 event (Fig. 7). Although simulated number concentrations are lower than re-

trieved and the PSD shapes not as narrow, the overall development of DWR trends with height is generated by the model's
520   standard physics schemes without requiring any special tuning. If model number concentrations are doubled prior to the for-
ward calculations, reflectivity is overestimated (not shown). We have therefore not tried to exactly match retrieved number
concentrations and ice PSD widths, also owing to weak constraints on ice crystal properties.

In summary, the bin model simulation corroborates the plausibility of scenarios capable of producing the unique signatures
observed during this event. DWR parameter space agreement with the observations could be reached in other sensitivity tests
525   where some vertical motion was introduced or in cases where the nudged sounding profile was slightly modified. However,
reaching these high (low) $DWR_{Ka,W}$ ($DWR_{X,Ka}$) values always required some compromises concerning the reflectivity aloft,
for example (as in this depicted simulation), thus emphasizing the difficulty to constrain ice properties with our limited obser-
vational dataset. Yet, the fact that similar results could be reached using somewhat varying configurations as long they allowed
narrow rimed ice PSD with diameters on the order of a few millimeters to be produced and developed, suggest that such cases
530   might occasionally occur over the Antarctic (or other polar regions). The frequency of occurrence of such scenarios will be
examined in future studies.

5   Conclusions

In this work, by exploiting the deployment of an unprecedented number of multi-wavelength active and passive remote sens-
ing systems (including triple-frequency radar measurements) in West Antarctica during the Atmospheric Radiation Measure-
535   ments West Antarctic Radiation Experiment (AWARE) field campaign, we find frequent occurrences of extremely high Ka-W
dual-wavelength ratios (DWR) coinciding with relatively low X-Ka dual-wavelength ratios taking place at unexpectedly low
temperatures of -20°C, in comparison to the mid-latitudes. These features are commonly interpreted as riming signatures and
pinpoint at unique ice processes over Antarctica, even if the limited amount of the triple frequency dataset collected during
AWARE does not allow drawing definite conclusions.
540   An extraordinary case study featuring a persistent layer with relatively modest amounts of supercooled liquid water pro-
ducing such unexpectedly strong triple-frequency radar signatures is analysed in greater detail. Since in situ observations are
lacking, the radar observations are exploited to retrieve the properties of the ice particles leading to these signatures. To this
aim, several state-of-the-art microphysics and scattering models (EM-MIC models) are used. The combination of the triple-
frequency radar reflectivities, the differential spectral width and a proxy of the ice particles fall velocities derived from the
545   Doppler spectra allows to constrain the ice particles microphysical properties. Results suggest that the fall velocity associated
with recent rimed aggregates EM-MIC models is too large, and a novel potentially more realistic EM-MIC model is therefore
proposed. Even if a non-negligible uncertainty remains on the size of the retrieved ice particles, results indicate that the ob-
served DWR signatures can only be explained by the combined effects of moderately rimed aggregates or similarly shaped
florid polycrystals and a narrow particle size distribution (PSD). More studies are needed to validate the retrieval algorithm
550   proposed here. This could be done either by cross-comparing the algorithm results with other techniques and/or by using in-situ

validation datasets from field campaigns (Leinonen et al., 2018; Mason et al., 2018; Battaglia et al., 2020b; Mroz et al., 2021; Nguyen et al., 2021).

Simulations of this case study performed with a 1D bin model confirm that, with the modest amount of supercooled liquid water, the triple frequency radar observations can be generally reproduced, provided that narrow PSDs are simulated. Such

555 narrow PSDs could be explained by two key factors: (i) the presence of a shallow homogeneous droplet or humidified aerosol freezing layer aloft seeding a supercooled liquid layer, and (ii) the absence of turbulent mixing throughout a stable polar atmosphere that sustains narrow PSDs, as hydrometeors grow from the nucleation region aloft to several millimeter ice particles, by vapor deposition and then riming.

This study illustrates that triple-frequency radar measurements can be used to infer detailed properties of precipitating ice

560 such as the PSD width or the degree of riming of ice particles. While the associated retrieval techniques are still at an exploratory stage, such information is crucial for improving our understanding of the role of ice phase in the water budget. Therefore, more observations and analysis involving triple-frequency radars are needed in the future.

Data availability. AWARE data were obtained from the U.S. DOE ARM Climate Research Facility https://www.archive.arm. gov (Atmospheric Radiation Measurement (ARM) user facility, 2014, 2015a, c, b).

565 *Author contributions.* ARM radars data analysis was made by FT and PK. Bin model simulations and their analysis were made by IS and AF. Interpretation and writing were shared between FT, IS, AB, SK and AF. RD provided the satellite data.

Competing interests. The authors declare that they have no conflict of interest.

Acknowledgements. This work was funded by the US Atmospheric System Research (grant no. DESC0017967). Contributions by SK were funded by the German Research Foundation (DFG) under grant KN 1112/2-1 as part of the Emmy-Noether Group "Optimal combination of

570 Polarimetric and Triple Frequency radar techniques for Improving Microphysical process understanding of cold clouds" (OPTIMIce).

References

Ackerman, A. S., Hobbs, P. V., and Toon, O. B.: A Model for Particle Microphysics, Turbulent Mixing, and Radiative Transfer in the Stratocumulus-Topped Marine Boundary Layer and Comparisons with Measurements, Journal of Atmospheric Sciences, 52, 1204 – 1236, https://doi.org/10.1175/1520-0469(1995)052<1204:AMFPMT>2.0.CO;2, https://journals.ametsoc.org/view/journals/atsc/
575   52/8/1520-0469_1995_052_1204_amfpmt_2_0_co_2.xml, 1995.

Atmospheric Radiation Measurement (ARM) user facility: Ka ARM Zenith Radar (KAZRMD), 2015-11-17 to 2017-01-02, ARM Mobile Facility (AWR) McMurdo Station Ross Ice Shelf, Antarctica; AMF2 (M1), https://doi.org/10.5439/1095601, compiled by I. Lindenmaier, N. Bharadwaj, K. Johnson, D. Nelson, B. Isom, J. Hardin, A. Matthews, T. Wendler and V. Castro. ARM Data Center. Data set accessed 2019-12-05 at http://dx.doi.org/10.5439/1095601, 2014.

580 Atmospheric Radiation Measurement (ARM) user facility: Marine W-Band (95 GHz) ARM Cloud Radar (MWACR), 2015-11-17 to 2016-03-20, ARM Mobile Facility (AWR) McMurdo Station Ross Ice Shelf, Antarctica; AMF2 (M1), https://doi.org/10.5439/1150242, compiled by I. Lindenmaier, N. Bharadwaj, K. Johnson, B. Isom, J. Hardin, A. Matthews, T. Wendler and V. Castro. ARM Data Center. Data set accessed 2019-12-05 at http://dx.doi.org/10.5439/1095601, 2015a.

Atmospheric Radiation Measurement (ARM) user facility: Balloon-Borne Sounding System (SONDEWNPN), 2015-11-30 to 2017-01-03,
585   ARM Mobile Facility (AWR) McMurdo Station Ross Ice Shelf, Antarctica; AMF2 (M1), https://doi.org/10.5439/1150303, compiled by E. Keeler, R. Coulter and J. Kyrouac. ARM Data Center. Data set accessed 2021-12-05 at http://dx.doi.org/10.5439/1021460, 2015b.

Atmospheric Radiation Measurement (ARM) user facility: X-Band Scanning ARM Cloud Radar (XSACRVPT), 2015-12-06 to 2016-07-15, ARM Mobile Facility (AWR) McMurdo Station Ross Ice Shelf, Antarctica; AMF2 (M1), https://doi.org/10.5439/1150303, compiled by I. Lindenmaier, N. Bharadwaj, K. Johnson, D. Nelson, B. Isom, J. Hardin, A. Matthews, T. Wendler and V. Castro. ARM Data Center. Data
590   set accessed 2021-12-05 at http://dx.doi.org/10.5439/1150303, 2015c.

Bailey, M. P. and Hallett, J.: A Comprehensive Habit Diagram for Atmospheric Ice Crystals: Confirmation from the Laboratory, AIRS II, and Other Field Studies, Journal of the Atmospheric Sciences, 66, 2888 – 2899, https://doi.org/10.1175/2009JAS2883.1, https://journals.ametsoc.org/view/journals/atsc/66/9/2009jas2883.1.xml, 2009.

Battaglia, A., Kollias, P., Dhillon, R., Roy, R., Tanelli, S., Lamer, K., Grecu, M., Lebsock, M., Watters, D., Mroz, K., Heymsfield, G., Li,
595   L., and Furukawa, K.: Spaceborne Cloud and Precipitation Radars: Status, Challenges, and Ways Forward, Reviews of Geophysics, 58, e2019RG000 686, https://doi.org/10.1029/2019RG000686, 2020a.

Battaglia, A., Tanelli, S., Tridon, F., Kneifel, S., Leinonen, J., and Kollias, P.: Satellite precipitation measurement, vol. 67 of *Adv.Global Change Res.*, chap. Triple-frequency radar retrievals, Springer, iSBN: 978-3-030-24567-2, 2020b.

Böhm, J. P.: Revision and clarification of "A general hydrodynamic theory for mixed-phase microphysics", Atmospheric research, 52, 167–
600   176, 1999.

Böhm, J. P.: Reply to Comment on"Revision and clarification of 'A general hydrodynamic theory for mixed-phase microphysics'[Bohm JP, 1999, Atmos. Res. 52, 167-176]", Atmospheric Research, 3, 289–293, 2004.

Borque, P., Luke, E., and Kollias, P.: On the unified estimation of turbulence eddy dissipation rate using Doppler cloud radars and lidars, Journal of Geophysical Research: Atmospheres, 121, 5972–5989, https://doi.org/https://doi.org/10.1002/2015JD024543, 2016.

605 Böhm, J. P.: A general hydrodynamic theory for mixed-phase microphysics. Part I: drag and fall speed of hydrometeors, Atmospheric Research, 27, 253–274, https://doi.org/https://doi.org/10.1016/0169-8095(92)90035-9, https://www.sciencedirect.com/science/article/pii/0169809592900359, 1992.

Carrasco, J. F. and Bromwich, D. H.: Climatological Aspects of Mesoscale Cyclogenesis over the Ross Sea and Ross Ice Shelf Regions of Antarctica, Monthly Weather Review, 122, 2405 – 2425, https://doi.org/10.1175/1520-0493(1994)122<2405:CAOMCO>2.0.CO;2, 1994.

Cesana, G., Kay, J. E., Chepfer, H., English, J. M., and de Boer, G.: Ubiquitous low-level liquid-containing Arctic clouds: New observations and climate model constraints from CALIPSO-GOCCP, Geophysical Research Letters, 39, https://doi.org/10.1029/2012GL053385, 2012.

Chenoli, S. N., Turner, J., and Samah, A. A.: A climatology of strong wind events at McMurdo station, Antarctica, International Journal of Climatology, 33, 2667–2681, https://doi.org/https://doi.org/10.1002/joc.3617, 2013.

Coggins, J. H. J., McDonald, A. J., and Jolly, B.: Synoptic climatology of the Ross Ice Shelf and Ross Sea region of Antarctica: k-means clustering and validation, International Journal of Climatology, 34, 2330–2348, https://doi.org/https://doi.org/10.1002/joc.3842, https://rmets.onlinelibrary.wiley.com/doi/abs/10.1002/joc.3842, 2014.

Dias Neto, J., Kneifel, S., Ori, D., Trömel, S., Handwerker, J., Bohn, B., Hermes, N., Mühlbauer, K., Lenefer, M., and Simmer, C.: The TRIple-frequency and Polarimetric radar Experiment for improving process observations of winter precipitation, Earth System Science Data, 11, 845–863, https://doi.org/10.5194/essd-11-845-2019, 2019.

Eloranta, E. W.: High spectral resolution lidar, in: Lidar: Range-Resolved Optical Remote Sensing of the Atmosphere, pp. 143–163, Springer New York, New York, NY, 2005.

Fitch, K. E. and Garrett, T. J.: Graupel Precipitating From Thin Arctic Clouds With Liquid Water Paths Less Than 50 g m-2, Geophysical Research Letters, 49, e2021GL094 075, https://doi.org/https://doi.org/10.1029/2021GL094075, 2022.

Fridlind, A. M., van Diedenhoven, B., Ackerman, A. S., Avramov, A., Mrowiec, A., Morrison, H., Zuidema, P., and Shupe, M. D.: A FIRE-ACE/SHEBA Case Study of Mixed-Phase Arctic Boundary Layer Clouds: Entrainment Rate Limitations on Rapid Primary Ice Nucleation Processes, Journal of the Atmospheric Sciences, 69, 365 – 389, https://doi.org/10.1175/JAS-D-11-052.1, https://journals.ametsoc.org/view/journals/atsc/69/1/jas-d-11-052.1.xml, 2012.

Garrett, T. J., Yuter, S. E., Fallgatter, C., Shkurko, K., Rhodes, S. R., and Endries, J. L.: Orientations and aspect ratios of falling snow, Geophysical Research Letters, 42, 4617–4622, https://doi.org/https://doi.org/10.1002/2015GL064040, 2015.

Grazioli, J., Lloyd, G., Panziera, L., Hoyle, C. R., Connolly, P. J., Henneberger, J., and Berne, A.: Polarimetric radar and in situ observations of riming and snowfall microphysics during CLACE 2014, Atmospheric Chemistry and Physics, 15, 13 787–13 802, https://doi.org/10.5194/acp-15-13787-2015, 2015.

Grazioli, J., Genthon, C., Boudevillain, B., Duran-Alarcon, C., Del Guasta, M., Madeleine, J.-B., and Berne, A.: Measurements of precipitation in Dumont d'Urville, Adélie Land, East Antarctica, The Cryosphere, 11, 1797–1811, https://doi.org/10.5194/tc-11-1797-2017, 2017.

Heymsfield, A. J.: A Comparative Study of the Rates of Development of Potential Graupel and Hail Embryos in High Plains Storms, Journal of the Atmospheric Sciences, 39, 2867–2897, https://doi.org/10.1175/1520-0469(1982)039<2867:ACSOTR>2.0.CO;2, 1982.

Heymsfield, A. J. and Westbrook, C. D.: Advances in the Estimation of Ice Particle Fall Speeds Using Laboratory and Field Measurements, Journal of the Atmospheric Sciences, 67, 2469 – 2482, https://doi.org/10.1175/2010JAS3379.1, 2010.

Heymsfield, A. J., Protat, A., Bouniol, D., Austin, R. T., Hogan, R. J., Delanoë, J., Okamoto, H., Sato, K., van Zadelhoff, G.-J., Donovan, D. P., and Wang, Z.: Testing IWC Retrieval Methods Using Radar and Ancillary Measurements with In Situ Data, Journal of Applied Meteorology and Climatology, 47, 135 – 163, https://doi.org/10.1175/2007JAMC1606.1, https://journals.ametsoc.org/view/journals/apme/47/1/2007jamc1606.1.xml, 2008.

Hogan, R. J. and Westbrook, C. D.: Equation for the Microwave Backscatter Cross Section of Aggregate Snowflakes Using the Self-Similar Rayleigh-Gans Approximation, Journal of Atmospheric Sciences, 71, 3292–3301, https://doi.org/10.1175/JAS-D-13-0347.1, 2014.

Hogan, R. J., Mittermaier, M. P., and Illingworth, A. J.: The retrieval of ice water content from radar reflectivity factor and temperature and its use in the evaluation of a mesoscale model, J. Appl. Meteorol., 45, 301–317, https://doi.org/10.1175/JAM2340.1, 2006.

Hogan, R. J., Honeyager, R., Tyynelä, J., and Kneifel, S.: Calculating the millimetre-wave scattering phase function of snowflakes using the self-similar Rayleigh-Gans Approximation, Quarterly Journal of the Royal Meteorological Society, 143, 834–844, https://doi.org/10.1002/qj.2968, 2017.

Jensen, E. J. and Ackerman, A. S.: Homogeneous aerosol freezing in the tops of high-altitude tropical cumulonimbus clouds, Geophysical Research Letters, 33, https://doi.org/https://doi.org/10.1029/2005GL024928, 2006.

Jensen, E. J., Toon, O. B., Tabazadeh, A., Sachse, G. W., Anderson, B. E., Chan, K. R., Twohy, C. W., Gandrud, B., Aulenbach, S. M., Heymsfield, A., Hallett, J., and Gary, B.: Ice nucleation processes in upper tropospheric wave-clouds observed during SUCCESS, Geophysical Research Letters, 25, 1363–1366, https://doi.org/https://doi.org/10.1029/98GL00299, 1998.

Jensen, E. J., Pfister, L., Ackerman, A. S., Tabazadeh, A., and Toon, O. B.: A conceptual model of the dehydration of air due to freeze-drying by optically thin, laminar cirrus rising slowly across the tropical tropopause, Journal of Geophysical Research: Atmospheres, 106, 17 237–17 252, https://doi.org/https://doi.org/10.1029/2000JD900649, 2001.

Karrer, M., Seifert, A., Siewert, C., Ori, D., von Lerber, A., and Kneifel, S.: Ice Particle Properties Inferred From Aggregation Modelling, Journal of Advances in Modeling Earth Systems, 12, e2020MS002 066, https://doi.org/https://doi.org/10.1029/2020MS002066, 2020.

Khvorostyanov, V. I. and Curry, J. A.: Fall Velocities of Hydrometeors in the Atmosphere: Refinements to a Continuous Analytical Power Law, Journal of the Atmospheric Sciences, 62, 4343 – 4357, https://doi.org/10.1175/JAS3622.1, 2005.

Kneifel, S. and Moisseev, D.: Long-Term Statistics of Riming in Nonconvective Clouds Derived from Ground-Based Doppler Cloud Radar Observations, Journal of the Atmospheric Sciences, 77, 3495–3508, https://doi.org/10.1175/JAS-D-20-0007.1, 2020.

Kneifel, S., Kulie, M. S., and Bennartz, R.: A triple-frequency approach to retrieve microphysical snowfall parameters, Journal of Geophysical Research: Atmospheres, 116, https://doi.org/10.1029/2010JD015430, 2011.

Kneifel, S., von Lerber, A., Tiira, J., Moisseev, D., Kollias, P., and Leinonen, J.: Observed relations between snowfall microphysics and triple-frequency radar measurements, J. Geophys. Res., 120, 6034–6055, https://doi.org/10.1002/2015JD023156, 2015.

Kneifel, S., Kollias, P., Battaglia, A., Leinonen, J., Maahn, M., Kalesse, H., and Tridon, F.: First observations of triple-frequency radar Doppler spectra in snowfall: Interpretation and applications, Geophys. Res. Lett., 43, 2225–2233, https://doi.org/10.1002/2015GL067618, 2016.

Kollias, P., Bharadwaj, N., Widener, K., Jo, I., and Johnson, K.: Scanning ARM Cloud Radars. Part I: Operational Sampling Strategies, Journal of Atmospheric and Oceanic Technology, 31, 569–582, https://doi.org/10.1175/JTECH-D-13-00044.1, 2014.

Kollias, P., Clothiaux, E. E., Ackerman, T. P., Albrecht, B. A., Widener, K. B., Moran, K. P., Luke, E. P., Johnson, K. L., Bharadwaj, N., Mead, J. B., Miller, M. A., Verlinde, J., Marchand, R. T., and Mace, G. G.: Development and Applications of ARM Millimeter-Wavelength Cloud Radars, Meteorological Monographs, 57, 17.1–17.19, https://doi.org/10.1175/AMSMONOGRAPHS-D-15-0037.1, 2016.

Kollias, P., Puigdomènech Treserras, B., and Protat, A.: Calibration of the 2007–2017 record of Atmospheric Radiation Measurements cloud radar observations using CloudSat, Atmospheric Measurement Techniques, 12, 4949–4964, https://doi.org/10.5194/amt-12-4949-2019, 2019.

Kollias, P., Bharadwaj, N., Clothiaux, E. E., Lamer, K., Oue, M., Hardin, J., Isom, B., Lindenmaier, I., Matthews, A., Luke, E. P., Giangrande, S. E., Johnson, K., Collis, S., Comstock, J., and Mather, J. H.: The ARM Radar Network: At the Leading Edge of Cloud and Precipitation Observations, Bulletin of the American Meteorological Society, 101, E588–E607, https://doi.org/10.1175/BAMS-D-18-0288.1, 2020.

Lane, T. P. and Sharman, R. D.: Gravity wave breaking, secondary wave generation, and mixing above deep convection in a three-dimensional cloud model, Geophysical Research Letters, 33, https://doi.org/https://doi.org/10.1029/2006GL027988, 2006.

685 Leinonen, J. and Szyrmer, W.: Radar signatures of snowflake riming: A modeling study, Earth and Space Science, 2, 346–358, https://doi.org/10.1002/2015EA000102, 2015.

Leinonen, J., Lebsock, M. D., Tanelli, S., Sy, O. O., Dolan, B., Chase, R. J., Finlon, J. A., von Lerber, A., and Moisseev, D.: Retrieval of snowflake microphysical properties from multifrequency radar observations, Atmos. Meas. Tech., 11, 5471–5488, https://doi.org/10.5194/amt-11-5471-2018, 2018.

690 Liu, J., Dedrick, J., Russell, L. M., Senum, G. I., Uin, J., Kuang, C., Springston, S. R., Leaitch, W. R., Aiken, A. C., and Lubin, D.: High summertime aerosol organic functional group concentrations from marine and seabird sources at Ross Island, Antarctica, during AWARE, Atmospheric Chemistry and Physics, 18, 8571–8587, https://doi.org/10.5194/acp-18-8571-2018, https://acp.copernicus.org/articles/18/8571/2018/, 2018.

Lohmann, U.: Can Anthropogenic Aerosols Decrease the Snowfall Rate?, Journal of the Atmospheric Sciences, 61, 2457–2468,
695 https://doi.org/10.1175/1520-0469(2004)061<2457:CAADTS>2.0.CO;2, 2004.

Lubin, D., Bromwich, D. H., Vogelmann, A. M., Verlinde, J., and Russell, L. M.: ARM West Antarctic Radiation Experiment (AWARE) Field Campaign Report, Tech. Rep. DOE/SC-ARM-17-028, U.S. Department of Energy, available at: https://www.arm.gov/publications/programdocs/doe-sc-arm-17-028.pdf (last access: 9 Novembre 2020), 2017.

Lubin, D., Zhang, D., Silber, I., Scott, R. C., Kalogeras, P., Battaglia, A., Bromwich, D. H., Cadeddu, M., Eloranta, E., Fridlind, A., Frossard,
700 A., Hines, K. M., Kneifel, S., Leaitch, W. R., Lin, W., Nicolas, J., Powers, H., Quinn, P. K., Rowe, P., Russell, L. M., Sharma, S., Verlinde, J., and Vogelmann, A. M.: AWARE: The Atmospheric Radiation Measurement (ARM) West Antarctic Radiation Experiment, Bulletin of the American Meteorological Society, https://doi.org/10.1175/BAMS-D-18-0278.1, 2020.

Maahn, M. and Löhnert, U.: Potential of Higher-Order Moments and Slopes of the Radar Doppler Spectrum for Retrieving Microphysical and Kinematic Properties of Arctic Ice Clouds, Journal of Applied Meteorology and Climatology, 56, 263 – 282,
705 https://doi.org/10.1175/JAMC-D-16-0020.1, 2017.

Maahn, M., Burgard, C., Crewell, S., Gorodetskaya, I. V., Kneifel, S., Lhermitte, S., Van Tricht, K., and van Lipzig, N. P. M.: How does the spaceborne radar blind zone affect derived surface snowfall statistics in polar regions?, Journal of Geophysical Research: Atmospheres, 119, 13,604–13,620, https://doi.org/10.1002/2014JD022079, 2014.

Mason, S. L., Chiu, C. J., Hogan, R. J., Moisseev, D., and Kneifel, S.: Retrievals of Riming and Snow Density From Vertically Pointing
710 Doppler Radars, J. Geophys. Res. Atm., 123, 13,807–13,834, https://doi.org/10.1029/2018JD028603, 2018.

Mason, S. L., Hogan, R. J., Westbrook, C. D., Kneifel, S., Moisseev, D., and von Terzi, L.: The importance of particle size distribution and internal structure for triple-frequency radar retrievals of the morphology of snow, Atmos. Meas. Tech., 12, 4993–5018, https://doi.org/10.5194/amt-12-4993-2019, 2019.

Matus, A. V. and L'Ecuyer, T. S.: The role of cloud phase in Earth's radiation budget, Journal of Geophysical Research: Atmospheres, 122,
715 2559–2578, https://doi.org/10.1002/2016JD025951, 2017.

Mioche, G., Jourdan, O., Ceccaldi, M., and Delanoë, J.: Variability of mixed-phase clouds in the Arctic with a focus on the Svalbard region: a study based on spaceborne active remote sensing, Atmospheric Chemistry and Physics, 15, 2445–2461, https://doi.org/10.5194/acp-15-2445-2015, 2015.

Mioche, G., Jourdan, O., Delanoë, J., Gourbeyre, C., Febvre, G., Dupuy, R., Monier, M., Szczap, F., Schwarzenboeck, A., and Gayet, J.-F.: Vertical distribution of microphysical properties of Arctic springtime low-level mixed-phase clouds over the Greenland and Norwegian seas, Atmospheric Chemistry and Physics, 17, 12 845–12 869, https://doi.org/10.5194/acp-17-12845-2017, 2017.

Moisseev, D., von Lerber, A., and Tiira, J.: Quantifying the effect of riming on snowfall using ground-based observations, Journal of Geophysical Research: Atmospheres, 122, 4019–4037, https://doi.org/10.1002/2016JD026272, 2017.

Monaghan, A. J., Bromwich, D. H., Powers, J. G., and Manning, K. W.: The Climate of the McMurdo, Antarctica, Region as Represented by One Year of Forecasts from the Antarctic Mesoscale Prediction System, Journal of Climate, 18, 1174 – 1189, https://doi.org/10.1175/JCLI3336.1, https://journals.ametsoc.org/view/journals/clim/18/8/jcli3336.1.xml, 2005.

Morrison, H., de Boer, G., Feingold, G., Harrington, J., Shupe, M. D., and Sulia, K.: Resilience of persistent Arctic mixed-phase clouds, Nature Geoscience, 5, 11–17, https://doi.org/10.1038/ngeo1332, 2012.

Mosimann, L.: An improved method for determining the degree of snow crystal riming by vertical Doppler radar, Atmospheric Research, 37, 305 – 323, https://doi.org/10.1016/0169-8095(94)00050-N, 1995.

Mroz, K., Battaglia, A., Nguyen, C., Heymsfield, A., Protat, A., and Wolde, M.: Triple-frequency radar retrieval of microphysical properties of snow, Atmospheric Measurement Techniques, 14, 7243–7254, https://doi.org/10.5194/amt-14-7243-2021, https://amt.copernicus.org/articles/14/7243/2021/, 2021.

Nguyen, C. M., Wolde, M., Battaglia, A., Nichman, L., Bliankinshtein, N., Haimov, S., Bala, K., and Schuettemeyer, D.: Coincident In-situ and Triple-Frequency Radar Airborne Observations in the Arctic, Atmospheric Measurement Techniques Discussions, 2021, 1–27, https://doi.org/10.5194/amt-2021-148, https://amt.copernicus.org/preprints/amt-2021-148/, 2021.

Ori, D., von Terzi, L., Karrer, M., and Kneifel, S.: snowScatt 1.0: Consistent model of microphysical and scattering properties of rimed and unrimed snowflakes based on the self-similar Rayleigh-Gans Approximation, Geoscientific Model Development Discussions, 2020, 1–33, https://doi.org/10.5194/gmd-2020-359, 2020.

Petäjä, T., O'Connor, E. J., Moisseev, D., Sinclair, V. A., Manninen, A. J., Väänänen, R., von Lerber, A., Thornton, J. A., Nicoll, K., Petersen, W., Chandrasekar, V., Smith, J. N., Winkler, P. M., Krüger, O., Hakola, H., Timonen, H., Brus, D., Laurila, T., Asmi, E., Riekkola, M.-L., Mona, L., Massoli, P., Engelmann, R., Komppula, M., Wang, J., Kuang, C., Bäck, J., Virtanen, A., Levula, J., Ritsche, M., and Hickmon, N.: BAECC: A Field Campaign to Elucidate the Impact of Biogenic Aerosols on Clouds and Climate, Bulletin of the American Meteorological Society, 97, 1909–1928, https://doi.org/10.1175/BAMS-D-14-00199.1, 2016.

Podglajen, A., Bui, T. P., Dean-Day, J. M., Pfister, L., Jensen, E. J., Alexander, M. J., Hertzog, A., Kärcher, B., Plougonven, R., and Randel, W. J.: Small-Scale Wind Fluctuations in the Tropical Tropopause Layer from Aircraft Measurements: Occurrence, Nature, and Impact on Vertical Mixing, Journal of the Atmospheric Sciences, 74, 3847 – 3869, https://doi.org/10.1175/JAS-D-17-0010.1, https://journals.ametsoc.org/view/journals/atsc/74/11/jas-d-17-0010.1.xml, 2017.

Protat, A., Delanoë, J., Bouniol, D., Heymsfield, A. J., Bansemer, A., and Brown, P.: Evaluation of Ice Water Content Retrievals from Cloud Radar Reflectivity and Temperature Using a Large Airborne In Situ Microphysical Database, Journal of Applied Meteorology and Climatology, 46, 557, https://doi.org/10.1175/JAM2488.1, 2007.

Rosenkranz, P. W.: Water vapor microwave continuum absorption: A comparison of measurements and models, Radio Sci., 33, 919–928, https://doi.org/10.1029/98RS01182, 1998.

Seifert, A., Leinonen, J., Siewert, C., and Kneifel, S.: The Geometry of Rimed Aggregate Snowflakes: A Modeling Study, Journal of Advances in Modeling Earth Systems, 11, 712–731, https://doi.org/10.1029/2018MS001519, 2019.

Shupe, M. D., Daniel, J. S., de Boer, G., Eloranta, E. W., Kollias, P., Long, C. N., Luke, E. P., Turner, D. D., and Verlinde, J.: A Focus On Mixed-Phase Clouds, Bulletin of the American Meteorological Society, 89, 1549–1562, https://doi.org/10.1175/2008BAMS2378.1, 2008.

Silber, I., Verlinde, J., Eloranta, E. W., Flynn, C. J., and Flynn, D. M.: HSRL Liquid cloud base height / MPL Liquid cloud base height, https://doi.org/10.5439/1438194, https://www.osti.gov/servlets/purl/1438194, 2018a.

760 Silber, I., Verlinde, J., Eloranta, E. W., Flynn, C. J., and Flynn, D. M.: Polar Liquid Cloud Base Detection Algorithms for High Spectral Resolution or Micropulse Lidar Data, Journal of Geophysical Research: Atmospheres, 123, 4310–4322, https://doi.org/https://doi.org/10.1029/2017JD027840, https://agupubs.onlinelibrary.wiley.com/doi/abs/10.1029/2017JD027840, 2018b.

Silber, I., Fridlind, A. M., Verlinde, J., Ackerman, A. S., Chen, Y.-S., Bromwich, D. H., Wang, S.-H., Cadeddu, M., and Eloranta, E. W.: Persistent Supercooled Drizzle at Temperatures Below -25 °C Observed at McMurdo Station, Antarctica, Journal of Geophysical Research:
765 Atmospheres, 124, 10 878–10 895, https://doi.org/10.1029/2019JD030882, 2019a.

Silber, I., Verlinde, J., Wang, S.-H., Bromwich, D. H., Fridlind, A. M., Cadeddu, M., Eloranta, E. W., and Flynn, C. J.: Cloud Influence on ERA5 and AMPS Surface Downwelling Longwave Radiation Biases in West Antarctica, Journal of Climate, 32, 7935 – 7949, https://doi.org/10.1175/JCLI-D-19-0149.1, https://journals.ametsoc.org/view/journals/clim/32/22/jcli-d-19-0149.1.xml, 2019b.

Silber, I., Fridlind, A. M., Verlinde, J., Ackerman, A. S., Cesana, G. V., and Knopf, D. A.: The prevalence of precipitation from polar su-
770 percooled clouds, Atmospheric Chemistry and Physics, 21, 3949–3971, https://doi.org/10.5194/acp-21-3949-2021, https://acp.copernicus. org/articles/21/3949/2021/, 2021.

Simmonds, I., Keay, K., and Lim, E.-P.: Synoptic Activity in the Seas around Antarctica, Monthly Weather Review, 131, 272 – 288, https://doi.org/10.1175/1520-0493(2003)131<0272:SAITSA>2.0.CO;2, 2003.

Stephens, G. L., Vane, D. G., Tanelli, S., Im, E., Durden, S., Rokey, M., Reinke, D., Partain, P., Mace, G. G., Austin, R., L'Ecuyer,
775 T., Haynes, J., Lebsock, M., Suzuki, K., Waliser, D., Wu, D., Kay, J., Gettelman, A., Wang, Z., and Marchand, R.: Cloud-Sat mission: Performance and early science after the first year of operation, Journal of Geophysical Research: Atmospheres, 113, https://doi.org/https://doi.org/10.1029/2008JD009982, 2008.

Stevens, D. E., Ackerman, A. S., and Bretherton, C. S.: Effects of Domain Size and Numerical Resolution on the Simula-tion of Shallow Cumulus Convection, Journal of the Atmospheric Sciences, 59, 3285 – 3301, https://doi.org/10.1175/1520-
780 0469(2002)059<3285:EODSAN>2.0.CO;2, https://journals.ametsoc.org/view/journals/atsc/59/23/1520-0469_2002_059_3285_eodsan_ 2.0.co_2.xml, 2002.

Testud, J., Oury, S., Black, R. A., Amayenc, P., and Dou, X.: The Concept of "Normalized" Distribution to Describe Raindrop Spectra: A Tool for Cloud Physics and Cloud Remote Sensing, Journal of Applied Meteorology, 40, 1118 – 1140, https://doi.org/10.1175/1520-0450(2001)040<1118:TCONDT>2.0.CO;2, 2001.

785 Tridon, F. and Battaglia, A.: Dual-frequency radar Doppler spectral retrieval of rain drop size distributions and entangled dynamics variables, J. Geophys. Res. Atm., 120, 5585–5601, https://doi.org/10.1002/2014JD023023, 2015.

Tridon, F., Battaglia, A., Chase, R. J., Turk, F. J., Leinonen, J., Kneifel, S., Mroz, K., Finlon, J., Bansemer, A., Tanelli, S., Heymsfield, A. J., and Nesbitt, S. W.: The Microphysics of Stratiform Precipitation During OLYMPEX: Compatibility Between Triple-Frequency Radar and Airborne In Situ Observations, J. Geophys. Res. Atm., 124, 8764–8792, https://doi.org/10.1029/2018JD029858, 2019.

790 Tridon, F., Battaglia, A., and Kneifel, S.: Estimating total attenuation using Rayleigh targets at cloud top: applications in multilayer and mixed-phase clouds observed by ground-based multifrequency radars, Atmospheric Measurement Techniques, 13, 5065–5085, https://doi.org/10.5194/amt-13-5065-2020, 2020.

Turk, F. J., Park, K.-W., Haddad, Z. S., Rodriguez, P., and Hudak, D. R.: Constraining CloudSat-based snowfall pro-
files using surface observations and C-band ground radar, Journal of Geophysical Research: Atmospheres, 116,
https://doi.org/https://doi.org/10.1029/2011JD016126, 2011.

von Lerber, A., Moisseev, D., Bliven, L. F., Petersen, W., Harri, A.-M., and Chandrasekar, V.: Microphysical Properties of Snow
and Their Link to Ze–S Relations during BAECC 2014, Journal of Applied Meteorology and Climatology, 56, 1561–1582,
https://doi.org/10.1175/JAMC-D-16-0379.1, 2017.

Weber, N. J., Lazzara, M. A., Keller, L. M., and Cassano, J. J.: The Extreme Wind Events in the Ross Island Region of Antarctica, Weather
and Forecasting, 31, 985 – 1000, https://doi.org/10.1175/WAF-D-15-0125.1, 2016.

Zawadzki, I., Fabry, F., and Szyrmer, W.: Observations of supercooled water and secondary ice generation by a vertically pointing X-band
Doppler radar, Atmospheric Research, 59-60, 343 – 359, https://doi.org/10.1016/S0169-8095(01)00124-7, 13th International Conference
on Clouds and Precipitation, 2001.